DOI: 10.1002/ ((please add manuscript number))
Article type: Full Paper

A Novel Bone Substitute with High Bioactivity, Strength and Porosity for Repairing Large and Load-Bearing Bone Defects

*Jiao Jiao Li, Colin R. Dunstan, Ali Entezari, Qing Li, Roland Steck, Siamak Saifzadeh, Ameneh Sadeghpour, John R. Field, Austin Akey, Martin Vielreicher, Oliver Friedrich, Seyed-Iman Roohani-Esfahani, Hala Zreiqat**

Dr. J. J. Li, A/Prof. C. R. Dunstan, Prof. H. Zreiqat
Biomaterials and Tissue Engineering Research Unit, School of Aerospace, Mechanical and Mechatronic Engineering, University of Sydney, Sydney, NSW 2006, Australia
E-mail: hala.zreiqat@sydney.edu.au
Dr. J. J. Li
Raymond Purves Bone and Joint Research Laboratories, Institute of Bone and Joint Research, Kolling Institute, Northern Sydney Local Health District, Faculty of Medicine and Health, University of Sydney, St Leonards, NSW 2065, Australia
Dr. J. J. Li, A/Prof. C. R. Dunstan, Prof. Q. Li, A. Sadeghpour, Prof. H. Zreiqat
Australian Research Council Training Centre for Innovative BioEngineering, Sydney, NSW 2006, Australia
A. Entezari, Prof. Q. Li
School of Aerospace, Mechanical and Mechatronic Engineering, University of Sydney, Sydney, NSW 2006, Australia
Dr. R. Steck, Dr. S. Saifzadeh
Medical Engineering Research Facility (MERF), Institute of Health and Biomedical Innovation (IHBI), Queensland University of Technology, Prince Charles Hospital Campus, Brisbane 4000, QLD, Australia
A. Sadeghpour
Allegra Orthopaedics Limited, Sydney, NSW 2000, Australia.
A/Prof. J. R. Field
Centre for Orthopaedic Trauma and Research, University of Adelaide, Adelaide, SA 5000, Australia
Dr. A. Akey
Center for Nanoscale Systems, Harvard University, Cambridge, MA 02138, USA
Dr. M. Vielreicher, Prof. O. Friedrich
Institute of Medical Biotechnology, Department of Chemical and Biological Engineering, Friedrich Alexander University of Erlangen-Nürnberg, Erlangen 91052, Germany
Dr. S.-I. Roohani-Esfahani
School of Chemistry, University of New South Wales, Kensington 2052, NSW, Australia
Prof. H. Zreiqat
Radcliffe Institute for Advanced Study, Harvard University, Cambridge, MA 02138, USA

Keywords: ceramic scaffolds, critical-sized bone defects, bone regeneration, bone graft substitutes, gahnite

To achieve adequate healing in large or load-bearing bone defects is highly challenging even with surgical intervention. The clinical standard of repairing bone defects using autologous or

allogeneic bone grafts has many drawbacks. We have developed a bioactive ceramic scaffold, strontium-hardystonite-gahnite or "Sr-HT-Gahnite" (a multi-component, calcium silicate-based ceramic), which when 3D printed combines high strength with outstanding bone regeneration ability. In this study, we assess the performance of purely synthetic, 3D printed Sr-HT-Gahnite scaffolds in repairing large and load-bearing bone defects. The scaffolds are implanted into critical-sized segmental defects in sheep tibia for 3 and 12 months, with autologous bone grafts used for comparison. The scaffolds induce substantial bone formation and defect bridging after 12 months, as indicated by X-ray, micro-computed tomography, histological and biomechanical analyses. Detailed analysis of the bone-scaffold interface using focused ion beam scanning electron microscopy and multiphoton microscopy show evidence of scaffold degradation and maturation of the newly formed bone. *In silico* modeling of strain energy distribution in the scaffolds reveal the importance of surgical fixation and mechanical loading on long-term bone regeneration. The clinical application of 3D printed Sr-HT-Gahnite scaffolds as a synthetic bone substitute can potentially improve the repair of challenging bone defects, and overcome the limitations of bone graft transplantation.

1. Introduction

Long bones of the body, particularly the femur and tibia, are the main structures responsible for load-bearing during daily activities and are crucial for skeletal mobility. Extensive bone loss due to trauma or disease is a major contributor to musculoskeletal disorders that lead to disability, frailty and reduced quality of life. A longstanding clinical problem is to achieve adequate healing in large or load-bearing bone defects, which is particularly challenging due to the impaired ability of bone to repair itself across a 'critical-sized' gap, generally 3cm or more in humans.[1] Even with surgical intervention, delayed healing or non-union occurs in 5–10% of bone fractures,[2] and the non-union of segmental bone defects approaches 100%.[3] Segmental defects in the long bones, often as a result of traumatic events or sports-related

injuries, are particularly common in young adults and are associated with substantially impaired mobility and function.[4] Autologous bone grafts are the current clinical standard for treating large bone defects, combining the essential criteria of high bioactivity and strength for inducing functional bone regeneration. However, despite excellent outcomes, the use of autologous bone grafts has been restricted by significant drawbacks relating to donor site morbidity, insufficient supply, and high graft resorption rate.[5,6] The alternative use of allogeneic bone grafts can address some of these drawbacks, but are associated with other issues including reduced bioactivity and strength due to processing, and poor integration with native bone.[7]

The search for an ideal bone graft substitute material to replace autologous and allogeneic bone grafts has drawn increasing interest over the last two decades, but a satisfactory solution has not yet been found. The criteria used to assess the properties of synthetic bone substitutes for clinical application are based on those exhibited by autologous bone grafts.[8] First, the substitute should be highly bioactive, with osteoconductive (can support bone formation on the material surface) and ideally osteoinductive (can actively induce new bone formation) properties, to promote bone formation without the need to add cells or growth factors. Second, the graft should be mechanically strong and provide prolonged support for tissue regeneration when implanted in load-bearing defects, and participate in withstanding physiological loads. Last, the graft should have the ability to be manufactured through a controlled process and possess a reproducible structure, together with high porosity and interconnectivity to ensure sufficient nutrient exchange and vascularization that are necessary for supporting bone formation and ongoing turnover.

Current synthetic bone substitutes for clinical use are dominated by bioceramics composed of calcium phosphates and bioactive glasses, which can at most partially satisfy two of the above listed criteria. Among the calcium phosphates, hydroxyapatite is the most stable and is not

highly bioactive,[9] while β-tricalcium phosphate and biphasic calcium phosphate lack mechanical strength at the range of porosities (50–90%) commonly required for bone regeneration.[10] Bioactive glasses generally have poor strength, and their bioactivity may be affected by the processing required to form porous scaffolds.[11] For these reasons, current clinical applications of bioceramic bone substitutes are limited to particulates for filling bone cavities and poorly interconnected blocks with low porosity for grafting small volumes of bone loss, typically at non load-bearing sites.[12] There is hence a critical need to develop novel synthetic graft materials that can properly address all of the essential criteria and lead to improved clinical treatment of highly challenging bone defects.

Over the past five decades, a wide range of synthetic materials have been developed in efforts to overcome the above limitations, but none of these have made the genuine transition from laboratory to clinic. Among those that have been tested in clinically relevant *in vivo* models, a popular formulation is hydroxyapatite combined with polycaprolactone (PCL) in various ratios,[13-16] as well as other calcium phosphate-based compositions.[17-19] Through fabrication using additive manufacturing techniques, these implants can generally satisfy the criterion for having a controlled structure with fully interconnected pores, although relatively low porosities of around 50% are typically required to maintain sufficient strength for load-bearing purposes.[15,18] A common challenge is the limited bioactivity of synthetic implants, with most studies indicating low or minimal bone formation in critical-sized defects, and the need to incorporate cells or growth factors to achieve appropriate healing.[13,14,16,19] This may be a limiting factor for the timely translation of such implants into clinical application, since the necessity to include biologics introduces additional issues such as donor variations in cell behavior, difficulties in determining the appropriate dosage and combination of growth factors, problems with diffusion of growth factors into adjacent tissues, and limited shelf life of the implant.

In response to these challenges, we combined multiple design strategies to develop a novel, multi-component bioceramic known as strontium-hardystonite-gahnite or "Sr-HT-Gahnite".[20] Sr-HT-Gahnite is a calcium silicate-based ceramic with a unique microstructure that forms during sintering, consisting of crystalline grains of strontium-hardystonite ($Sr–Ca_2ZnSi_2O_7$) with a wetting glass phase at the grain boundaries, embedded within which are submicron gahnite crystals ($ZnAl_2O_4$).[20,21] We have also developed the technology to produce 3D printed Sr-HT-Gahnite scaffolds with high porosity (70%) and full interconnectivity (100%).[22] To date, we have demonstrated that these scaffolds possess mechanical strength matching cortical bone, combined with outstanding bioactivity and ability to induce osteogenesis *in vitro* and *in vivo* (in rabbits).[20-23] This study is the next step in progressing the Sr-HT-Gahnite scaffolds to clinical use, by validating their performance in a clinically relevant large animal model. Here, we tested the *in vivo* ability of 3D printed Sr-HT-Gahnite scaffolds to induce natural regeneration in critical-sized segmental defects in the long bones of sheep over one year, without the addition of cells or growth factors. We assessed the structural, biomechanical and biological outcomes of defect repair, and related these outcomes to observations of microscopic material-tissue interactions and modeling of strain energy distribution in the scaffolds. The results showed substantial bone formation and defect bridging, indicating that Sr-HT-Gahnite scaffolds could be used as an improved synthetic bone substitute, and potentially contribute towards solving the clinical dilemma associated with bone graft transplantation. This study also revealed important information regarding the influence of factors such as bone-implant interactions and mechanical loading on long-term bone repair using synthetic substitutes.

2. Results

2.1. Scaffold implantation, post-operative observations and radiographic analysis

Sr-HT-Gahnite scaffolds used in this study were produced by 3D printing, with dimensions fitting the created defects (**Figure 1A**). The scaffolds had porosity of 70% and were fully interconnected, with average pore sizes of 1.1 mm and strut sizes of 0.5 mm, as measured using micro-computed tomography (μ-CT).

The study was conducted using a total of 28 sheep, each with a critical-sized, 3 cm long mid-diaphyseal defect created in the tibia of one hindlimb (**Figure 1B**). The sheep were divided into two cohorts of 14 animals each for the 3 month and 12 month time points. In each cohort, the sheep received either a 3D printed Sr-HT-Gahnite scaffold implant (n=8) or autologous bone graft (ABG) prepared from the removed tibial bone (n=6). The defect was stabilized using a modified 10-hole Dynamic Compression Plate, which was retained until euthanasia.

All animals resumed load-bearing of the experimental limb following surgical recovery. With the exception of one animal in the scaffold group, which was euthanized at 18 weeks due to welfare concerns not associated with the experimental defect, all other experimental animals remained in good health over the duration of the study. All animals receiving the Sr-HT-Gahnite scaffolds tolerated the implants well, without clinically significant inflammatory reactions or implant failure over the 12 month implantation period. The animals were euthanized at 13 weeks (8 scaffolds, 6 ABG) or 52 weeks (7 scaffolds, 6 ABG) after surgery. Necropsy revealed stable constructs in all animals and no evidence of post-operative complications.

X-ray images of the Sr-HT-Gahnite scaffold group (12 month cohort) were taken at 3 month intervals over the implantation period (**Figure 1C**). The defect borders were less distinguishable at 9 and 12 months, and some remodeling of the defect site was evident to restore the original shape of the limb. Clinical union was observed at the bone-implant interface beyond 6 months, indicating good integration between the scaffold and host bone.

2.2. μ-CT analysis at 3 and 12 months

μ-CT was used to determine the distribution and volume of new bone in tibial explants containing the Sr-HT-Gahnite scaffold or ABG, at 3 and 12 months post-implantation. For the scaffold group, at least partial bridging of the defect was achieved in all samples at both 3 and 12 months. Complete defect bridging by newly formed bone was observed for one of eight scaffolds at 3 months, and five of seven scaffolds at 12 months. Representative reconstructed images of longitudinal and transverse cross-sections showed that bone formation at 3 and 12 months within the scaffold-implanted defects followed the same distinct patterns, with new bone partly distributed along the defect periphery superficial to the scaffold, and partly within the porous structure of the scaffold (**Figure 2A**). At 12 months, there was a higher volume of newly formed bone within the scaffold pores at all locations along the length of the defect compared to at 3 months. The patterns of bone distribution suggested that the Sr-HT-Gahnite scaffold induced rapid bone growth peripheral to the implant to bridge the defect, concurrent with slower bone infiltration into the scaffold pores from the defect edges to fill the empty spaces. All samples in the ABG group showed complete bridging at both 3 and 12 months (**Figure S1**), as expected.

The volume of new bone within the defect was determined using quantitative image analysis, and was defined as all material above the threshold determined for bone mineral. The scaffold group showed a lower volume of new bone compared to the ABG group at 3 months, but achieved comparable values to the ABG group at 12 months (**Figure 2B**). The scaffold group also exhibited a trend to an increase in new bone volume from 3 to 12 months, which was consistent with the reconstructed cross-sectional images and indicated ongoing repair processes during the implantation period. The volume of scaffold material within the defect was measured

at 3 and 12 months, and found to be similar to the pre-implantation scaffold volume, indicating the occurrence of only low levels of macroscopic scaffold degradation (**Figure 2C**).

2.3. Histological analysis at 3 and 12 months

Tibial explants containing the Sr-HT-Gahnite scaffold or ABG were sectioned and stained to allow histological assessment of the nature and quality of new tissue present in the defect at 3 and 12 months post-implantation. Representative images of whole sections (**Figure 3A**) showed new bone formation advancing into the porous structure of the Sr-HT-Gahnite scaffold from both ends of the defect at 3 months, but had not yet occupied the middle section of the scaffold. At 12 months, two samples showed complete filling of the spaces within the Sr-HT-Gahnite scaffold with newly formed bone that was continuous across the entire defect. There was some variation in the amount of new bone present in different scaffold samples at both 3 and 12 months, but all showed substantial bone infiltration into the scaffold. There was no evidence of chronic inflammation or fibrous capsule formation surrounding the scaffold in any of the samples. Defects implanted using ABG showed complete bridging at 12 months, with partial reforming of the original bone architecture that comprised a cortical bone shell and the creation of an endocortical marrow space.

At 3 months post-implantation (**Figure 3B, C**), new bone tissue present within the scaffold was dominated by woven bone (purple or dark blue), with a disorganized appearance and frequently encompassing multiple types of immature tissue. In some areas, tissue adjacent to the scaffold was found to contain mineralized bone surrounding a center region of mineralized cartilage, with the latter exhibiting metachromasia (different color) when stained using toluidine blue due to its high proteoglycan content (**Figure 3B**). The woven bone was lined by osteoid (blue edge) on one end, indicating active bone formation in the region immediately adjacent to the scaffold.

In other areas of the scaffold particularly at increasing distance from the defect edges, immature woven bone was commonly observed with a highly disorganized appearance (**Figure 3C**).

At 12 months post-implantation (**Figure 3D–G**), new bone within the scaffold underwent increased maturation compared to at 3 months, exhibiting the characteristic appearance of lamellar bone and a cortical-like architecture, as well as evidence of ongoing and active bone remodeling. An image taken near the defect edge showed the interface between original cortical bone and newly formed bone (**Figure 3D**). The original bone was inactive, highly mineralized lamellar bone that was organized into distinct layers. The new bone surrounding the scaffold struts was lamellar bone that was richly mineralized but exhibited a disorganized arrangement, with no specific orientation. The majority of this new bone stained a darker color with toluidine blue compared to the original cortical bone, likely due to its higher proteoglycan content. This was particularly evident in the new bone immediately adjacent to the scaffold struts, which stained dark purple and was lined with a blue border of unmineralized osteoid, indicative of active bone formation. Similar evidence of active bone formation was observed within an advancing front of new bone (dark purple lined with blue borders), which was progressing upwards to fill the spaces within the scaffold. This process of active bone formation within the scaffold was better visualized with the Goldner's trichrome stain (**Figure 3E**). Newly formed mineralized bone (teal) was seen surrounding the scaffold struts, and was lined with a border of osteoid (dark orange) in the area immediately adjacent to the ceramic. An advancing front of bone formation was also evident, where unmineralized bone matrix (dark orange) was present between the mineralized bone and invading into the loose connective tissue (light orange). This was indicative of a continuous process of primary bone formation that would then undergo secondary remodeling to form mature mineralized bone, which would eventually fill a significant proportion of the pore spaces within the scaffold.

Closer examination of the new bone within the scaffold revealed longitudinal and transverse sections of osteons, consisting of a Haversian canal surrounded by concentric layers of lamellar bone (**Figure 3F**). These Haversian osteons, surrounding a central blood vessel, provided evidence of active remodeling to form cortical-like, vascularized bone. This Haversian remodeling was better observed in sections stained for tartrate-resistant acid phosphatase (TRAP; red stain) to show osteoclast-specific activity (**Figure 3G**). The osteoclasts were localized in the bone immediately adjacent to the scaffold, suggesting that the ceramic supported material-cell interactions that might contribute to remodeling of the surrounding bone.

In comparison, the defects implanted with ABG at 12 months post-implantation showed a less distinct interface between the original cortical bone and newly formed bone (**Figure S2**). Highly mineralized lamellar bone was present throughout the defect, although the bone became less well organized with increasing distance from the edges of the defect. There was some evidence of ongoing remodeling in the middle of the defect, compared to mostly inactive bone towards the defect edges. A thin border of ongoing bone formation along the defect periphery was present.

2.4. Histomorphometric analysis at 3 and 12 months

Histomorphometric analysis was used to quantitatively assess the extent of bone bridging across the defect, and the composition of new tissue formed within the defect, for samples containing the Sr-HT-Gahnite scaffold or ABG. The extent of bone bridging across the defect was calculated as the percentage of total defect length covered by new bone (**Figure 4A**). Two samples from the ABG group were randomly selected to perform histological and histomorphometric analyses at each time point, all of which showed complete defect bridging. For the Sr-HT-Gahnite scaffold group, complete bridging was achieved in one of eight samples at 3 months and five of seven samples at 12 months, which was consistent with the μ-CT data.

The mean percentage of defect bridging in the scaffold group increased significantly over time, from 48% at 3 months to 83% at 12 months. The composition of new tissue within the defect was quantitatively assessed at 12 months using Goldner's trichrome stained sections of samples from the Sr-HT-Gahnite scaffold and ABG groups (**Figure 4B**). The areas occupied by soft tissue and mineralized bone were expressed as percentages of total empty space within the defect. The scaffold group showed almost complete (80%) filling of the defect with new tissue, which was comparable to the ABG group (95%). The composition of this new tissue exhibited a higher ratio of mineralized bone to soft tissue in the ABG group compared to the scaffold group. There is potential for some of the soft tissue in the scaffold to be replaced by mineralized bone over longer time periods, due to evidence from the stained sections showing continuous invasion of the soft tissue by newly formed bone.

2.5. Focused ion beam scanning electron microscopy (FIB-SEM) analysis at 3 and 12 months

FIB-SEM analysis was performed on the unstained histological sections of tibial explants containing the Sr-HT-Gahnite scaffold, at 3 and 12 months post-implantation to allow detailed observations of the implant-bone interface. Regions of interest were selected to contain a clear view of a scaffold strut, surrounded by newly formed bone and highly cellular loose connective tissue (**Figure 5A, B**). At lower magnification in backscatter SEM imaging, the scaffold appeared white and was surrounded by a darker border, which was a zone depleted of certain elements due to ion leaching from the ceramic. Surrounding the scaffold strut was a diffuse layer of carbon-rich loose connective tissue (dark grey), outside which was mineralized lamellar bone containing many osteocyte lacunae. Comparing the images taken at 3 and 12 months revealed several differences at the implant-bone interface. At 3 months, the structure of the ceramic was well-preserved with no visible surface irregularities. The ring of loose connective tissue surrounding the scaffold was relatively thick, and the adjacent lamellar bone exhibited a

low degree of organization. At 12 months, the surface contour of the ceramic was less smooth and contained many fragmented edges. The darker border around the bulk ceramic had variable thickness along its circumference. The surrounding ring of loose connective tissue had decreased in thickness, and the adjacent lamellar bone had a much more organized appearance. Bone closest to the scaffold had grown in tightly packed, smooth concentric layers, and all of the bone appeared to have a higher degree of mineralization compared to that at 3 months. These observations suggested an ongoing scaffold degradation process, with ion leaching from the borders of the ceramic causing a gradual reduction in scaffold size, which then mediated soft tissue infiltration and its eventual replacement by mineralized bone. This was consistent with the histological observations that bone formation and remodeling were occurring more actively in the areas immediately adjacent to the scaffold struts.

X-ray elemental mapping of the image taken at 12 months showed the distribution of Ca, Al, Zn, C, P and O (**Figure 5C**). The center of the scaffold strut contained mainly Ca, Al, Zn and O, which was consistent with the ceramic composition. The ceramic border was rich in Al and O, but contained very little Ca and Zn, suggesting that Ca and Zn were the main ions leaching from the ceramic during its initial degradation. The dark material surrounding the ceramic contained large amounts of C and O, suggesting a highly cellular layer of loose connective tissue. The adjacent bone was dominated by Ca and P, which confirmed the presence of mature lamellar bone with high mineral content. The C elemental map showed many small spots in the bone with positions corresponding to voids in the Ca and P elemental maps, which likely represented osteocytes nesting within lacunae in the mineralized bone matrix.

FIB cross-sectioning allowed visualization of the implant-bone interface in nanoscale detail (**Figure 5D, E**). At both 3 and 12 months, the interface showed loose connective tissue (black) in close contact with the disrupted border of the ceramic. This disrupted border, which appeared

as a darker border around the bulk ceramic at lower magnification, was actually a zone of destruction where parts of the ceramic had disintegrated. At 12 months, the disrupted border had a greater thickness than at 3 months, and disintegration of the ceramic was more prominent. The loose connective tissue remained on the outside of the disrupted border at 3 months, but was able to infiltrate inside the border at 12 months and had reached the level of the bulk ceramic. This provided evidence for continuous degradation of the scaffold and gradual invasion by newly formed tissue.

2.6. Multiphoton microscopy analysis at 3 and 12 months

Multiphoton microscopy analysis was performed on the unstained histological sections of tibial explants containing the Sr-HT-Gahnite scaffold, at 3 and 12 months post-implantation to observe the organization of the bone extracellular matrix (**Figure 6**). Regions of interest were selected at different points along the section to include (1) the original bone, (2) new bone within the scaffold near the defect edge, and (3) new bone within the scaffold near the middle of the defect. The sections were imaged to specifically visualize the morphology and distribution of collagen type I fibers in the bone tissue around and within the scaffold implant. The 3 and 12 month sections showed a similar pattern in the arrangement of collagen fibers along the length of the defect. In the original bone outside the defect (region 1), the collagen fiber network was densely packed and highly organized, with a layered morphology that was characteristic of mature lamellar bone. The circular structures likely represented Haversian canals that formed a part of the osteons found in cortical bone. In the new bone within the scaffold near the defect edge (region 2), the collagen fibers were not aligned as in the original bone, but some organization into a layered morphology was evident particularly at 12 months. In contrast, new bone within the scaffold near the middle of the defect contained collagen fibers that were loosely packed with a low degree of organization, indicating the presence of immature tissue.

Comparing the appearance of collagen fibers in the bone at 3 and 12 months, at similar locations along the defect revealed increased bone formation and maturation between the two time points. In region 2, collagen in the bone at 12 months was organized into somewhat aligned fiber bundles, with a concentric arrangement that was reminiscent of the newly formed, mineralized lamellar bone seen in the histology images. In the same region at 3 months, the collagen network was less well organized and fiber alignment was only observed in discrete areas, indicating the presence of mainly woven rather than lamellar bone at this time. In region 3, the collagen fibers were quite densely packed at 12 months but had random orientations, which was characteristic of woven bone, compared to at 3 months where they were sparsely distributed and possibly indicating the presence of loose connective tissue rather than bone. The increase in density and degree of organization of the collagen fibers from the middle to the edge of the defect, and also from 3 to 12 months, suggested gradual removal and replacement of the initially formed immature bone with more mature new bone. It is likely that following scaffold implantation, woven bone is formed first and continually invades the loose connective tissue or empty spaces within the scaffold, progressing from the edges of the defect towards the middle. Over time, this immature bone is remodeled into mineralized lamellar bone that bears increasing resemblance to the original cortical bone, particularly near the defect edges.

2.7. Biomechanical testing at 3 and 12 months

Biomechanical testing was performed on tibial explants containing the Sr-HT-Gahnite scaffold or ABG, at 3 and 12 months post-implantation. At the 3 month time point, only two of the eight samples in the scaffold group were tested, as the remaining samples did not achieve sufficient stability for testing following plate removal. Biomechanical testing was performed on all samples in the scaffold group at 12 months, and all samples in the ABG group at 3 and 12 months.

The torsional stiffness (**Figure 7A**) and maximum torque (**Figure 7B**) of test samples implanted with the Sr-HT-Gahnite scaffold or ABG were determined, and normalized against values obtained for the contralateral, intact tibia. Relative torsional stiffness and maximum torque were lower for the scaffold group compared to ABG at both 3 and 12 months, although statistical analysis could not be performed at 3 months due to the small sample number in the scaffold group. At 12 months, the scaffold group achieved average values of 40% for torsional stiffness and 20% for maximum torque relative to the intact tibia, and exhibited some inter-sample variation with two of the samples reaching peak values of 70–80% for torsional stiffness and 30–40% for maximum torque. The scaffold and ABG groups both showed large increases in torsional stiffness and maximum torque from 3 to 12 months.

2.8. Strain energy of implanted scaffolds at 12 months

Mathematical modeling for all defects implanted with the Sr-HT-Gahnite scaffold for 12 months was performed *in silico* to understand the influence of mechanical loading on healing outcomes. The total elastic strain energy, which reflects the pattern of biomechanical stimulation, was quantified in a cross-section located in the center of each scaffold, in the same approximate location as the histological sections cut from the explants. X-ray images of scaffold-implanted defects at the 12 month time point indicated that there was some variation in the arrangement of the fixation plate and screws in each animal, which could result in different patterns of mechanical loading being transferred to the scaffold (**Figure 8**, top panel). Another source of variation was the quality of the bone-implant interface, with some visible gaps being present in samples 3, 5 and 6. A computational model mimicking the *in vivo* loading regime under walking condition was created for each sample, taking into consideration the location of the scaffold and the arrangement of the fixation construct, as determined from the X-ray images. These models enabled prediction of the total strain energy by simulating the

pattern of load transfer into the scaffold. The numerical results were then compared with the pattern of new bone formation in each sample observed in the stained histological sections (**Figure 8**, middle panel).

The total elastic strain energy in the longitudinal cross-section at the center of each scaffold (**Figure 8**, bottom panel) is shown in the same orientation as the corresponding histological section. A direct correlation is evident between the total strain energy and the amount and pattern of new bone formed in each defect. In samples 1 and 2, significant strain energy was evenly distributed over the majority of the cross-section, due to the non-rigid fixation of screws immediately adjacent to the sample. Stress shielding effects were therefore minimal, resulting in an even distribution of mechanical stimuli in the scaffold. This was matched by histological observations of complete defect bridging and large amounts of mineralized bone formation within the scaffold throughout the length of the defect. For samples 3 and 4, even strain energy was only found on the right side of the scaffold. On the left side in the region near the plate, zero strain energy was generated due to stress shielding, where the completely rigid screw fixation caused the majority of the load to be transferred through the plate. Accordingly, complete bone bridging was found on the right side of the scaffold in the histological sections, while the scaffold area on the left side was completely filled with soft tissue. For sample 5, non-zero strain energy was only found in the top left corner, corresponding to mineralized bone formation just in this region. The zero strain energy in the rest of the cross-section was possibly the combined effect of stress shielding due to rigid fixation, and a gap in the bone-scaffold interface on the top right. For samples 6 and 7, the scaffold was incompletely filled with soft tissue and contained minimal bone, which matched the zero strain on the left side of the cross-section but was not explained by high strain energy on the right side. Transverse μ-CT cross-sections revealed a fracture in sample 6 and some scaffold collapse in sample 7 (**Figure S3**), possibly affecting proper load transfer and hence reducing bone formation in the scaffold.

Nevertheless, significant bone bridging along the scaffold periphery was still present in these samples, but were not located in the center plane and hence were not intersected by the histological section.

These results collectively suggested that new bone formation proceeded optimally in defects with physiological levels of significant and evenly distributed loads. Uneven strain distribution or low strain due to improper load transfer or implant instability, which might result from variations in surgical fixation, could have considerable negative impacts on bone healing.

3. Discussion

Due to the increasing global incidence of bone injuries and the drawbacks experienced with autologous and allogeneic bone grafts, there is an urgent need for the development of improved synthetic bone substitutes and their efficient translation into clinical applications.[24] However, there are significant difficulties in developing a synthetic graft that simultaneously satisfies the regenerative requirements of bone, including bioactivity and ability to promote osteogenesis, mechanical properties sufficient for load-bearing, and high porosity and interconnectivity, with the practical requirements for clinical use and surgical handling, such as the ability to be manufactured with controlled geometry and high reproducibility, and capacity to be used as an off-the-shelf implant without needing to incorporate biologics for efficacy. In this study, we present the preclinical evaluation of a bioactive ceramic implant composed of Sr-HT-Gahnite in the repair of a highly challenging, critical-sized segmental defect in the tibia of sheep over 12 months, without the addition of cells or growth factors. We show that the Sr-HT-Gahnite scaffold implant has potential to satisfy the requirements for a synthetic bone substitute, with the ability to achieve significant healing through defect bridging and new bone formation, as assessed through radiographic, μ-CT, histological and biomechanical analyses, as well as

detailed characterization of the bone-implant interface through FIB-SEM and multiphoton microscopy, and mathematical modeling of mechanical loading on the implant and fixation construct.

The implanted Sr-HT-Gahnite scaffolds were very well tolerated by all animals over the 12 month study period. The scaffolds showed a strong ability to induce rapid bridging of the critical-sized defect, with complete bridging being achieved in one animal at 3 months, and in 70% of the animals at 12 months, as confirmed by the μ-CT and histomorphometric data. In addition to defect bridging peripheral to the implant, large amounts of new bone formation were found within the scaffold pores. The μ-CT data indicated that at 12 months, the volume of mineralized bone in defects implanted with the Sr-HT-Gahnite scaffold was comparable to those implanted with ABG. Interestingly, histomorphometric analysis at 12 months indicated that the total amount of new tissue formed within the defect area was similar between the scaffold and ABG groups, but the scaffold group had a comparatively lower ratio of mineralized bone to soft tissue. A possible reason for this difference between the outcomes of μ-CT and histomorphometric analyses is that μ-CT measurements were based on thresholding for mineralized bone over the whole sample, including bone formed peripheral to the implant, while histomorphometric measurements were based on one longitudinal cross-section taken from the center of each sample, which only included bone ingrowth into the implants. Since the Sr-HT-Gahnite scaffold induced rapid bone bridging to occur completely or partially across the defect peripheral to the implant, accompanied by the slower ingrowth of new bone through the scaffold pores, sections containing the center of the scaffold were expected to contain the least amount of mineralized bone in comparison to the other areas. Nevertheless, the histological evidence suggested that active bone formation and remodeling activities were ongoing and had not ceased at 12 months.

The outcomes of histological analysis and multiphoton microscopy indicated ongoing maturation and remodeling of the new bone formed within the Sr-HT-Gahnite scaffolds. The scaffolds appeared to possess both osteoconductive and osteoinductive properties, being able to not only support bone growth surrounding the implant and bone bridging on the periphery of the defect, but also induce significant invasion of new bone through the scaffold pores from the edges towards the center of the defect. As bone formation advanced into the scaffold, woven bone with a relatively disorganized structure was initially formed at a rapid rate, which constituted the majority of the new bone found within the defect at 3 months. By 12 months, the woven bone had been largely replaced by lamellar bone that was continuous across the entire defect in some samples. This lamellar bone was highly mineralized and exhibited a well-organized, cortical-like structure containing features of mature bone such as Haversian osteons and lamellar bone. The interface between new bone and ceramic struts of the scaffold appeared to be separated by a small gap in most instances, which was filled with a thin layer of soft tissue with no evidence of ongoing chronic inflammation or fibrous encapsulation of the implant. Osteoclast activity localized in the bone surrounding the ceramic suggested that the scaffold might be inducing active bone remodeling in its vicinity. This ongoing remodeling was necessary for bone maturation, resulting in the observed transition from woven bone near the defect center to earlier formed lamellar bone near the defect interface with original bone, which was verified by the arrangement and morphology of bone collagen visualized through multiphoton microscopy. Progressing from the center of the defect to the boundaries, the collagen network in the newly formed bone within the scaffold changed from a mostly random arrangement without a distinct orientation to a highly organized arrangement with layered morphology. The ability of the Sr-HT-Gahnite scaffold to support secondary remodeling following primary bone formation, through processes analogous to natural fracture healing, provides evidence for its high bioactivity.[25] These processes are necessary for the regeneration

of anatomically-similar bone tissue to facilitate long-term defect healing and sustained load-bearing.

Observations from FIB-SEM provided additional insights into the mechanisms of Sr-HT-Gahnite degradation and its influence on bone formation at the bone-implant interface. At both 3 and 12 months, there was no evidence of ceramic fretting surrounding the scaffold struts. Instead, degradation occurred at the ceramic surface through a two-step process, first by the leaching of Ca and Zn ions, followed by the slower removal of a highly disrupted, Al-rich border. At 12 months, this border was observed to increase in thickness and allow the infiltration of loose connective tissue. The release of Ca and Zn into the spaces surrounding the scaffold might be one of the mechanisms contributing to the osteoinductivity of the scaffold, by creating a richly mineralized environment that promoted the chemotaxis and osteogenic differentiation of osteoprogenitor cells.[26,27] While high concentrations of Al ions have been associated with osteomalacia and impaired bone remodeling,[28] elemental mapping in this study showed low concentrations of Al ions only on the outer surfaces of the scaffold, and no detectable amounts in the surrounding bone or soft tissues. These observations suggested that trace amounts of Al ions were released from the scaffold during its degradation and were physiologically removed, which eliminates possible concerns regarding toxic build-up of aluminum within the defect site. Elemental mapping also suggested that the scaffold struts were wrapped by a layer of highly cellular, loose connective tissue rather than directly interfacing with the newly formed bone. From 3 to 12 months, the cellular layer had decreased in thickness and the bone immediately adjacent to it had been remodeled into a more organized structure. Taken together with the histological observations, the likely process of bone formation within the Sr-HT-Gahnite scaffold was ceramic degradation causing the ingrowth of soft tissue, followed by replacement of the soft tissue with woven bone that was gradually converted into mature mineralized bone. Compared to bioactive ceramics that cause direct abutment of newly

formed bone to the implant surface,[25,29] the ability of the Sr-HT-Gahnite scaffold to maintain a cellular layer between the ceramic and new bone might be beneficial for long-term healing. Rather than being incorporated into the newly formed bone, the scaffold can facilitate ongoing cell-mediated ceramic degradation through the cellular layer, which is accompanied by active bone formation and remodeling adjacent to the implant.[30]

Other than structural healing of the defect with cortical-like bone, the Sr-HT-Gahnite scaffolds also achieved considerable functional restoration of the implanted limb at 12 months. The scaffolds possessed pre-implantation compressive strength that was within the range of values reported for cortical bone,[22] which was sufficient for supporting physiological loads immediately post-implantation and throughout the duration of the study. Although the scaffold group did not reach the same biomechanical properties as the ABG group, the values obtained at 3 and 12 months had greatly outperformed other scaffold-only implants tested as bone graft substitutes in similar ovine defect models.[13,14,16,25] The scaffold-implanted defects showed a large increase in biomechanical properties from 3 to 12 months, suggesting a gradual strengthening process that was consistent with the maturation of new bone observed through histology and multiphoton microscopy. Slow *in vivo* degradation of the scaffold was advantageous for long-term defect healing, by facilitating physiological load transfer over extended periods of time, thereby providing ongoing mechanical support and stimulation for bone growth and remodeling to occur.

Other than characteristics of the scaffold itself, the method of surgical implantation and fixation probably plays an equally significant part in influencing the outcomes of bone regeneration. It is long known that mechanical strains generated from loads placed on a scaffold are intimately linked to cellular responses and tissue regeneration,[31] and mechanical loading can act as an independent stimulator in bone healing.[18] The choice of fixation device can affect stress

shielding in the implant, thereby altering the patterns of strain distribution and having a direct impact on the outcomes of bone regeneration in clinically relevant defects.[32] As observed in this study, the rigidity of the fixation system and the quality of the bone-implant interface had profound effects on subsequent implant loading. This led to inter-sample variations in the healing outcomes, where implants with the most even strain distribution also had the highest biomechanical properties and greatest amount of bone formation, which were comparable to the results obtained using autologous bone grafts. These outcomes indicate that long-term implant stability and minimal stress shielding are essential for producing satisfactory healing in load-bearing long bones.

One of the limitations of this study was that the cylindrical Sr-HT-Gahnite scaffolds did not allow proper remodeling into anatomically-similar long bone with a cortical shell and endocortical marrow space. This limitation can be addressed in the future by 3D printing the scaffold in the shape of a hollow tube to replicate the native anatomy. The implanted scaffold can then exist as a semi-permanent implant to provide support for ongoing defect repair and bone remodeling. To minimize inter-sample variations in bone regeneration and ensure consistent and optimal healing, future studies should compare surgical implantation and fixation methods for maximizing treatment outcomes using the Sr-HT-Gahnite scaffold. A practical limitation of this study was that the same specimen from each animal was used for biomechanical testing, μ-CT imaging, and histological and histomorphometric analyses (in this sequence), to avoid the need to use multiple animals for different evaluation methods. Biomechanical testing might have resulted in spiral fractures through the specimens, which were clearly identifiable in some of the histological sections, such as the 12 month ABG section in Figure 3A. These fractures might have affected the macroscopic appearance of the specimen sections, but did not influence the microscopic analysis of tissue structure and morphology.

Detailed quantitative histomorphometric analyses were conducted only on regions not affected by the fractures.

The findings of this study suggest that 3D printed Sr-HT-Gahnite scaffolds have capacity to induce complete bone regeneration and defect healing in a highly challenging, critical-sized segmental defect that may not normally heal even with surgical intervention, without the need to incorporate cells or growth factors. To date, this achievement has never been observed for scaffold-only implants used as synthetic bone substitutes in clinically relevant defect models. Mathematical modeling revealed that surgical placement and appropriate implant fixation had equal importance as the inherent implant characteristics in maintaining long-term implant stability, seamless bone-implant integration, and physiological load transfer, factors which all had a potentially profound effect on the outcomes of bone healing.

4. Conclusion

With consistent and optimized surgical implantation techniques, Sr-HT-Gahnite scaffolds may have significant potential for clinical use as a purely synthetic bone substitute that can match the structural and functional outcomes of bone regeneration achieved with autologous bone grafts. The ability to produce off-the-shelf, cost-effective and patient-specific Sr-HT-Gahnite scaffolds, which are highly bioactive and able to induce complete healing in large or load-bearing bone defects, will bring significant potential to augment or substitute current surgical approaches for bone repair using autologous or allogeneic bone grafts.

5. Experimental Section

Fabrication of Sr-HT-Gahnite scaffolds: All reagents were purchased from Sigma-Aldrich, USA unless otherwise specified. Precursor ceramic powder for producing 3D printed Sr-HT-Gahnite scaffolds was prepared by mixing strontium-hardystonite (Sr–$Ca_2ZnSi_2O_7$) powder,

prepared using the sol-gel method, with 15 wt% aluminum oxide (Al_2O_3) powder, as previously described.[20] The powder was ground using a ball mill machine (Retsch PM 400, Germany) to obtain median particle sizes of 1 μm.

Sr-HT-Gahnite scaffolds with rectangular pore geometry were fabricated by 3D printing, as previously described.[22] Briefly, the ink was formulated by dispersing the precursor ceramic powder in a water-based organic solution. The ink was printed through a 600 μm custom-made nozzle using a robotic deposition device (Hyrel 3D, USA). A controlled heat treatment was used to decompose the organic materials in the printed scaffolds and sinter the ceramic particles to form dense struts. The unique microstructure of Sr-HT-Gahnite scaffolds forms during this process, consisting of strontium-hardystonite grains (Sr–$Ca_2ZnSi_2O_7$) and a glass phase at the grain boundaries containing submicron gahnite crystals ($ZnAl_2O_4$). The green samples were heated at 1°C/min to 450°C, followed by densification at 1250°C for 3 hours. The prepared scaffolds were cylindrical (diameter 20 mm, height 30 mm), with porosity of 70% and fully interconnected pores.

Surgical procedures for creation and implantation of critical-sized segmental defects in sheep tibia: All procedures were approved by the animal ethics committee at the Queensland University of Technology, Brisbane, Australia (approval number 1400000025). A critical-sized defect was created in the right tibia of 28 Merino wethers (weight 45.6 ± 5.7 kg, age 3-4 years), according to previously described and well-established methods.[33] Briefly, during surgery under general anesthesia, aseptic conditions and using a bimodal analgesics regime, a 3 cm segment of the mid-diaphyseal tibia was removed through a medial approach, and the defect was stabilized using a modified 10-hole Dynamic Compression Plate (Synthes, Switzerland). The defect was filled with either a 3D printed Sr-HT-Gahnite scaffold (n=16), or autologous bone graft composed of morselized cortical bone prepared from the 3 cm full-

thickness segments removed from the tibia (n=12), and the surgical wound was closed in layers. After surgery, a full-length fiberglass cast (Delta-Lite Plus, BSN medical) was applied to the operated limb to offer protection from excessive loading during the first 4 weeks of healing. Following cast removal, the animals were allowed to mobilize freely for the remaining duration of the study. X-ray images (Philips Veradius, Royal Philips, The Netherlands) were taken immediately post-operation, and then at 6 weeks, 3 months, 6 months, 9 months and 12 months. At the 3 month and 12 month time points, half of the animals from each group were euthanized, and the experimental limbs were explanted for further processing and analysis.

Biomechanical testing: Following sacrifice, the experimental and contralateral tibiae of each animal were explanted, and the fixation plate and screws were carefully removed from the experimental limb. For each sample, both tibial ends were embedded in dental acrylic (Palapress, Heraeus Kulzer, Germany), and the sample was then mounted in a biaxial mechanical testing machine (Instron 8874, Instron, Norwood MA, USA). The torsional stiffness and maximum torque were determined in internal rotation at an angular velocity of 0.5°/s. Results from the experimental tibiae were normalized against values obtained for the contralateral, intact tibiae to account for inter-individual differences. The samples were fixed in 10% neutral buffered formalin before further processing.

Micro-computed tomography (μ-CT): Prior to implantation, two of the Sr-HT-Gahnite scaffolds were scanned in a μ-CT scanner (μCT40, Scanco Medical, Bassersdorf, Switzerland). The X-ray tube was operated at 70 kV and 114 μA with 200 ms integration time, resulting in a voxel size of 36 μm. The scaffolds were segmented using a lower threshold of 1328.2 mg HA/ccm from the scans, and their morphological parameters were determined using the scanner's software (μCT Evaluation v6.6, Scanco Medical, Bassersdorf, Switzerland).

Following biomechanical testing of the tibial samples, the mid-diaphyseal section of each sample containing the defect was prepared for μ-CT. To determine new bone formation in the defect zone, scanning of the samples was performed using the same equipment and procedures as described above. Newly formed bone was distinguished from the scaffold material using a lower threshold of 508.1 mg HA/ccm and an upper threshold of 1328.2 mg HA/ccm, both with a Gaussian filter of sigma 1.8 and support of 3.0 using the scanner's software (μCT Evaluation v6.6).

Histological and histomorphometric analyses: Following μ-CT evaluation, the tibial samples were processed for histology. Samples were dehydrated through graded ethanol, cleared in xylene, and embedded in methyl methacrylate resin (Technovit 9100, Kulzer, Germany). Longitudinal thick sections (>250 μm thickness) were cut from each sample using a diamond saw (EXAKT, USA), and ground sections (30–50 μm thickness) were obtained through grinding (EXAKT microgrinder) and polishing (Tegramin polisher, Struers). The sections were stained using toluidine blue or Goldner's trichrome, and visualized using a Zeiss Axio Imager 2 microscope (Carl Zeiss, Germany). To visualize tartrate-resistant acid phosphatase (TRAP) enzyme activity, the sections were stained using a TRAP Staining Kit (Cosmo Bio, Japan), prior to counter-staining using toluidine blue.

Histomorphometric measurements were performed using a Goldner's trichrome stained section from each sample, and quantified using the Osteomeasure software (OsteoMetrics, USA). The defect area in each section was selected by defining the proximal and distal defect boundaries according to discontinuities in the structure of the lamellar bone (**Figure S4**). If bone bridging across the defect was incomplete, the percentage bridging was calculated by measuring the distance of penetration into the defect area by newly formed mineralized bone from both proximal and distal defect boundaries, and dividing by the total length of the defect area. The

areas occupied by soft tissue (orange) and mineralized bone (teal) in the total defect area were quantified using the software.

Focused ion beam scanning electron microscopy (FIB-SEM): Unstained histological sections were sputter-coated with 50 nm of amorphous carbon for charge dissipation. Focused ion beam (FIB) cross-sectioning and scanning electron microscopy (SEM) were performed using an FEI Helios 660 Dual-Beam FIB-SEM. The FIB was operated at 30 kV accelerating voltage and 9.5 nA probe current for coarse milling, with final polishing performed at 0.79 nA. SEM imaging was performed either at 20 kV using a photodiode backscatter detector, or at 3 kV in field-immersion mode using an in-column backscatter detector. For FIB processing, a protective layer of Pt was deposited in-situ to minimize curtaining effects and prevent surface erosion.

Multiphoton microscopy: Unstained histological sections were imaged without pre-labeling using two-photon microscopy. A TriMScope II (LaVision BioTec, Germany) was used, which was based on a Nikon Eclipse Ti-E inverted stage and equipped with an ultra-short pulsed Ti:Sa laser ($t < 150$ fs, repetition rate: 80 MHz; Chameleon Vision II, Coherent, USA), with dispersion pre-compensation and tunable wavelengths (λ=710-980 nm). Laser excitation occurred at λ=810 nm. The signals were collected using a 40× UV-vis-IR water immersion objective (LD C-apochromat, N.A.: 1.1, WD: 0.62; Zeiss, Germany) and separated by a dichroic mirror (460DCXR, Chroma Technology, USA). Wavelengths >460 nm were derived from cellular autofluorescence (AF) and detected in channel 1 (not shown). Wavelengths <460 nm were reflected, blocked using a bandpass filter (405/20, Chroma), and recorded as Second Harmonic Generation signals (SHG) from collagen-I fiber networks in channel 2. Detection occurred with high-sensitivity GaAsP photomultipliers (H7422-40, Hamamatsu Photonics, Japan), which were mounted in non-descanned configuration close to the back aperture of the

objective. The laser intensities and detector voltages were adapted for optimal signal quality in both channels. Images were analyzed using Fiji software (NIH, USA).

Mathematical modeling of strain energy: Mathematical modeling of total elastic strain energy in the implanted Sr-HT-Gahnite scaffolds was performed by reconstructing a μ-CT based sheep tibia model, and inserting a computer aided design scaffold model to closely mimic the *in vivo* placement of the scaffold in the bone defect and arrangement of the fixation device in each animal. Finite element analysis was performed on each sheep tibia model, and the total elastic strain energy was presented by taking a longitudinal cross-section at the center of the scaffold. Detailed computational modeling methods (**Figure S5**) are included in the Supporting Information.

Statistical analysis: Data were represented as mean ± standard deviation. The significance of differences between groups was assessed using a t-test with $p < 0.05$ taken to indicate significance. For box plots, data were represented as median, first quartile, and third quartile, with the error bars indicating maximum and minimum values.

Supporting Information
Supporting Information is available from the Wiley Online Library or from the author.

Acknowledgements
The authors thank the following staff from the Queensland University of Technology: the Medical Engineering Research Facility (MERF) for veterinary assistance and technical support, the Central Analytical Research Facility for assistance in conducting the histological analyses, and Dr Caroline Grant for donating the μ-CT scans of the sheep tibia. The authors acknowledge the following funding sources: The Australian Research Council (IC170100022), the Australian National Health and Medical Research Council (APP1107470 and APP1120249), and the Rebecca L. Cooper Medical Research Foundation, Australia; Center for Nanoscale Systems, a member of the National Nanotechnology Coordinated Infrastructure Network and a part of Harvard University, supported by the National Science Foundation (NSF Award No. 1541959), USA; Friedrich-Alexander University Erlangen-Nürnberg, supported by the Emerging Fields Initiative ADVENDO LIFE, Germany, and the German Academic Exchange Service and

Universities Australia mobility exchange grant scheme, Germany/Australia; the AO Foundation (Project No. S-14-97R), Switzerland.

Received: ((will be filled in by the editorial staff))
Revised: ((will be filled in by the editorial staff))
Published online: ((will be filled in by the editorial staff))

References

[1] C. A. Garrido, S. E. Lobo, F. M. Turibio, R. Z. LeGeros, *Int. J. Biomater.* **2011**, DOI: 10.1155/2011/129727.

[2] J. I. Dawson, R. O. C. Oreffo, *Arch. Biochem. Biophys.* **2008**, *473*, 124-131.

[3] P. R. Stafford, B. L. Norris, *Injury* **2010**, *41, Suppl 2*, S72-S77.

[4] K. A. Alberts, G. Loohagen, H. Einarsdottir, *Injury* **1999**, *30*, 519-523.

[5] E. D. Arrington, W. J. Smith, H. G. Chambers, A. L. Bucknell, N. A. Davino, *Clin. Orthop. Relat. Res.* **1996**, *329*, 300-309.

[6] J. C. Banwart, M. A. Asher, R. S. Hassanein, *Spine* **1995**, *20*, 1055-1060.

[7] A. S. Greenwald, S. D. Boden, V. M. Goldberg, Y. Khan, C. T. Laurencin, R. N. Rosier, *J. Bone Jt. Surg., Am. Vol.* **2001**, *83A*, S98-S103.

[8] Y. Liu, J. Lim, S.-H. Teoh, *Biotechnol. Adv.* **2013**, *31*, 688-705.

[9] S. Samavedi, A. R. Whittington, A. S. Goldstein, *Acta Biomater.* **2013**, *9*, 8037-8045.

[10] A. J. Wagoner Johnson, B. A. Herschler, *Acta Biomater.* **2011**, *7*, 16-30.

[11] Q. Fu, E. Saiz, M. N. Rahaman, A. P. Tomsia, *Mater. Sci. Eng., C* **2011**, *31*, 1245-1256.

[12] J. J. Li, D. L. Kaplan, H. Zreiqat, *J. Mater. Chem. B* **2014**, *2*, 7272-7306.

[13] A. Berner, J. C. Reichert, M. A. Woodruff, S. Saifzadeh, A. J. Morris, D. R. Epari, M. Nerlich, M. A. Schuetz, D. W. Hutmacher, *Acta Biomater.* **2013**, *9*, 7874-7884.

[14] A. Cipitria, J. C. Reichert, D. R. Epari, S. Saifzadeh, A. Berner, H. Schell, M. Mehta, M. A. Schuetz, G. N. Duda, D. W. Hutmacher, *Biomaterials* **2013**, *34*, 9960-9968.

[15] A. E. Jakus, A. L. Rutz, S. W. Jordan, A. Kannan, S. M. Mitchell, C. Yun, K. D. Koube, S. C. Yoo, H. E. Whiteley, C.-P. Richter, R. D. Galiano, W. K. Hsu, S. R. Stock, E. L. Hsu, R. N. Shah, *Sci. Transl. Med.* **2016**, *8*, 358ra127.

[16] J. C. Reichert, A. Cipitria, D. R. Epari, S. Saifzadeh, P. Krishnakanth, A. Berner, M. A. Woodruff, H. Schell, M. Mehta, M. A. Schuetz, G. N. Duda, D. W. Hutmacher, *Sci. Transl. Med.* **2012**, *4*, 141ra93.

[17] C. Harms, K. Helms, T. Taschner, I. Stratos, A. Ignatius, T. Gerber, S. Lenz, S. Rammelt, B. Vollmar, T. Mittlmeier, *Int. J. Nanomed.* **2012**, *7*, 2883.

[18] S. Reitmaier, A. Kovtun, J. Schuelke, B. Kanter, M. Lemm, A. Hoess, S. Heinemann, B. Nies, A. Ignatius, *J. Orthop. Res.* **2017**, *36*, 106-117.

[19] J. R. Field, M. McGee, R. Stanley, G. Ruthenbeck, T. Papadimitrakis, A. Zannettino, S. Gronthos, S. Itescu, *Vet. Comp. Orthop. Traumatol.* **2011**, *24*, 113-121.

[20] S. I. Roohani-Esfahani, C. R. Dunstan, J. J. Li, Z. Lu, B. Davies, S. Pearce, J. Field, R. Williams, H. Zreiqat, *Acta Biomater.* **2013**, *9*, 7014-7024.

[21] S.-I. Roohani-Esfahani, Y. Chen, J. Shi, H. Zreiqat, *Mater. Lett.* **2013**, *107*, 378-381.

[22] S.-I. Roohani-Esfahani, P. Newman, H. Zreiqat, *Sci. Rep.* **2016**, *6*, 19468.

[23] J. J. Li, S.-I. Roohani-Esfahani, K. Kim, D. L. Kaplan, H. Zreiqat, *J. Tissue Eng. Regener. Med.* **2017**, *11*, 1741-1753.

[24] A. Bigham-Sadegh, A. Oryan, *Int. Wound J.* **2014**, *12*, 238-247.

[25] J. J. Li, S.-I. Roohani-Esfahani, C. R. Dunstan, T. Quach, R. Steck, S. Saifzadeh, P. Pivonka, H. Zreiqat, *Biomed. Mater.* **2016**, *11*, 015016.

[26] A. M. C. Barradas, H. A. M. Fernandes, N. Groen, Y. C. Chai, J. Schrooten, J. van de Peppel, J. P. T. M. van Leeuwen, C. A. van Blitterswijk, J. de Boer, *Biomaterials* **2012**, *33*, 3205-3215.

[27] M. M. Dvorak, D. Riccardi, *Cell Calcium* **2004**, *35*, 249-255.

[28] V. Sansone, D. Pagani, M. Melato, *Clin Cases Miner Bone Metab* **2013**, *10*, 34-40.

[29] J. J. Li, A. Akey, C. R. Dunstan, M. Vielreicher, O. Friedrich, D. C. Bell, H. Zreiqat, *Adv. Healthcare Mater.* **2018**, *7*, 1800218.

[30] C. Kunert-Keil, F. Scholz, T. Gedrange, T. Gredes, *Ann. Anat.* **2015**, *199*, 79-84.

[31] D. P. Byrne, D. Lacroix, J. A. Planell, D. J. Kelly, P. J. Prendergast, *Biomaterials* **2007**, *28*, 5544-5554.

[32] A.-M. Pobloth, S. Checa, H. Razi, A. Petersen, J. C. Weaver, K. Schmidt-Bleek, M. Windolf, A. Á. Tatai, C. P. Roth, K.-D. Schaser, G. N. Duda, P. Schwabe, *Sci. Transl. Med.* **2018**, *10*, eaam8828.

[33] J. C. Reichert, D. R. Epari, M. E. Wullschleger, S. Saifzadeh, R. Steck, J. Lienau, S. Sommerville, I. C. Dickinson, M. A. Schütz, G. N. Duda, D. W. Hutmacher, *Tissue Eng., Part B* **2010**, *16*, 93-104.

[34] W. R. Taylor, B. M. Poepplau, C. König, R. M. Ehrig, S. Zachow, G. N. Duda, M. O. Heller, *J. Orthop. Res.* **2011**, *29*, 567-571.

[35] H.-C. Spatz, E. J. O'Leary, J. F. V. Vincent, *Proc. Biol. Sci.* **1996**, *263*, 287-294.

[36] A. Entezari, S.-I. Roohani-Esfahani, Z. Zhang, H. Zreiqat, C. R. Dunstan, Q. Li, *Sci. Rep.* **2016**, *6*, 28816.

[37] A. Entezari, Z. Zhang, A. Sue, G. Sun, X. Huo, C.-C. Chang, S. Zhou, M. V. Swain, Q. Li, *J. Mech. Behav. Biomed. Mater.* **2018**, DOI: 10.1016/j.jmbbm.2018.08.034.

[38] B. Hassani E. Hinton, *Comput. Struct.* **1998**, *69*, 707-717.

[39] J. E. Cadman, S. Zhou, Y. Chen, Q. Li, *J. Mater. Sci.* **2013**, *48*, 51-66.

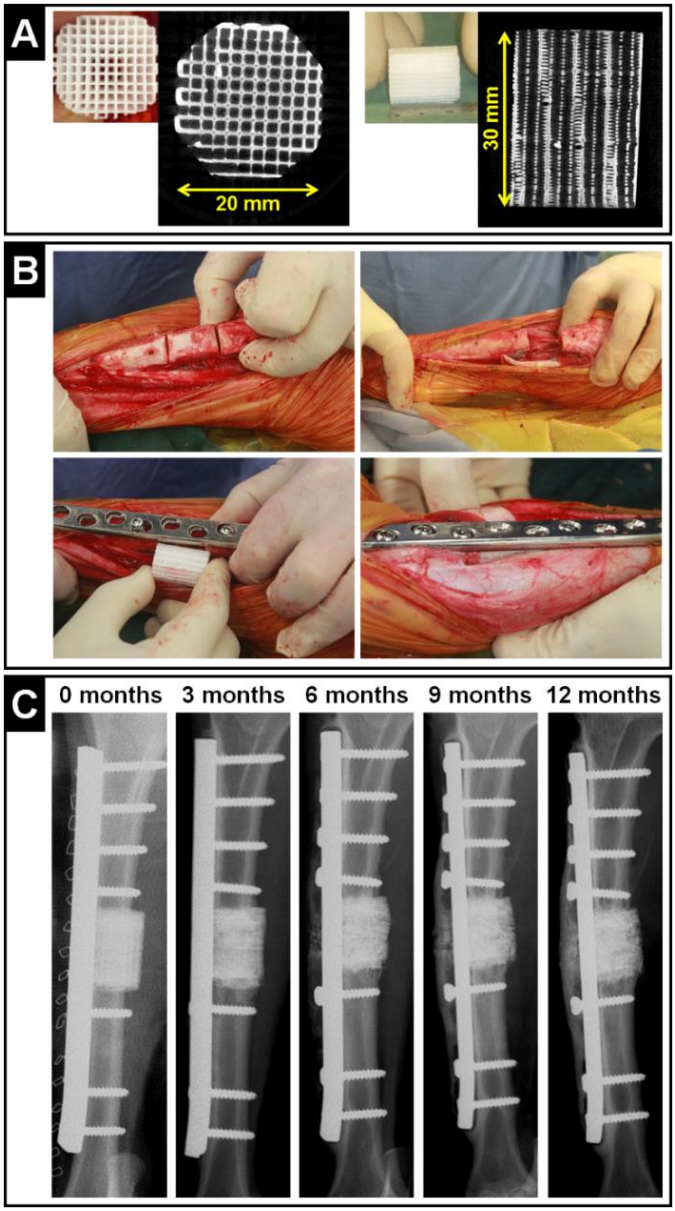

Figure 1. Sr-HT-Gahnite scaffold implant, surgical procedure, and post-operative X-ray images. **(A)** 3D printed Sr-HT-Gahnite scaffolds were used for implantation. The scaffolds had controlled geometry and a highly porous and fully interconnected structure, as shown macroscopically and through μ-CT imaging. The scaffolds were manufactured with dimensions matching the defect size in the sheep tibia. **(B)** Surgical procedure for implanting the Sr-HT-Gahnite scaffold into the bone defect. A critical-sized, 3cm long mid-diaphyseal defect was created in the tibia of the experimental animal. The defect was stabilized using a modified 10-hole Dynamic Compression Plate, and the scaffold was implanted into the defect by press-fitting. For defects implanted with autologous bone graft, the excised tibial bone segment was morselized using a bone mill to generate autologous bone chips, which were packed into the defect. **(C)** Representative X-ray images taken over the duration of the 12 month *in vivo* study, showing the critical-sized tibial defect treated using the Sr-HT-Gahnite scaffold.

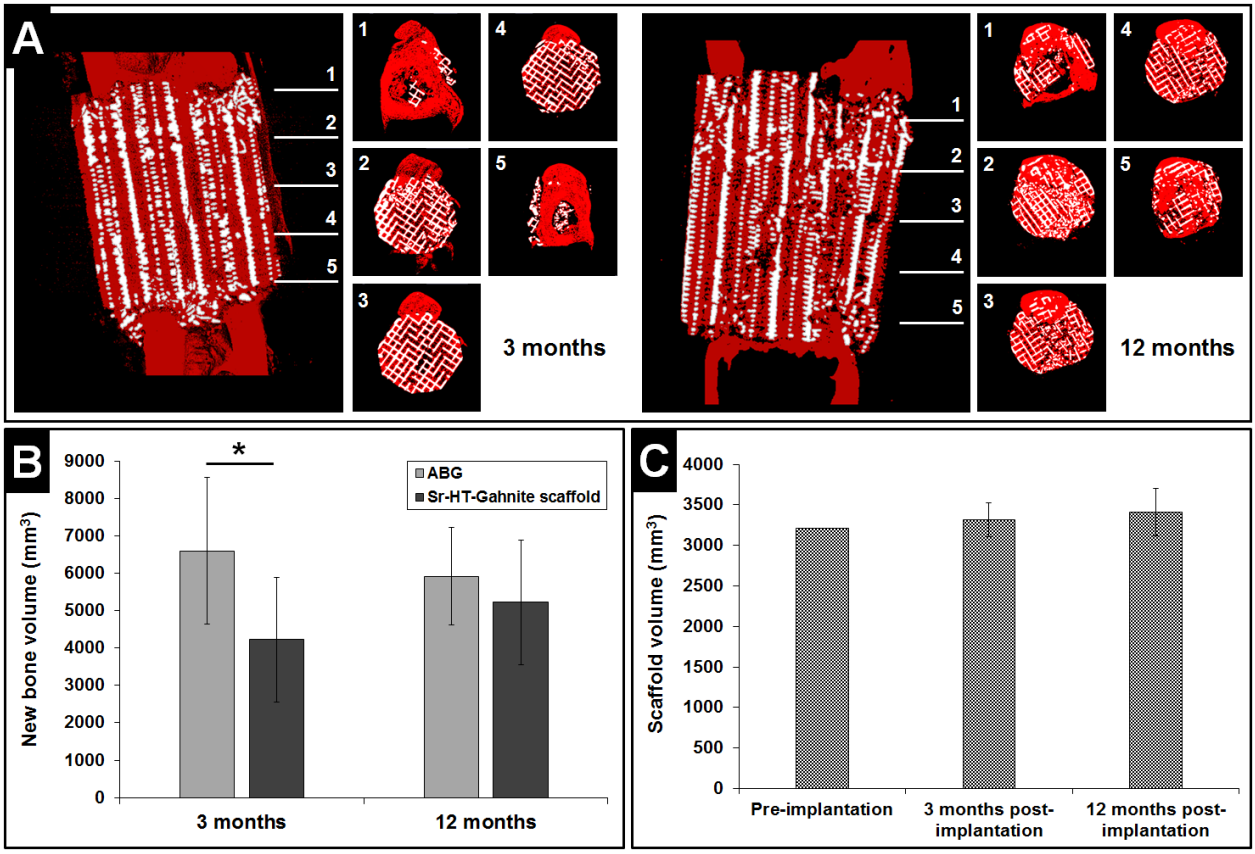

Figure 2. μ-CT analysis of new bone distribution and volume at 3 and 12 months. **(A)** Representative reconstructed images of longitudinal and transverse cross-sections of defects implanted with the Sr-HT-Gahnite scaffold at 3 and 12 months. Red = bone, white = scaffold. **(B)** Volume of new bone at 3 and 12 months for defects implanted with the Sr-HT-Gahnite scaffold (n=8 at 3 months, n=7 at 12 months) or ABG (n=6). *$p < 0.05$, two-tailed t-test. **(C)** Volume of scaffold material within the defect over the 12 month implantation period.

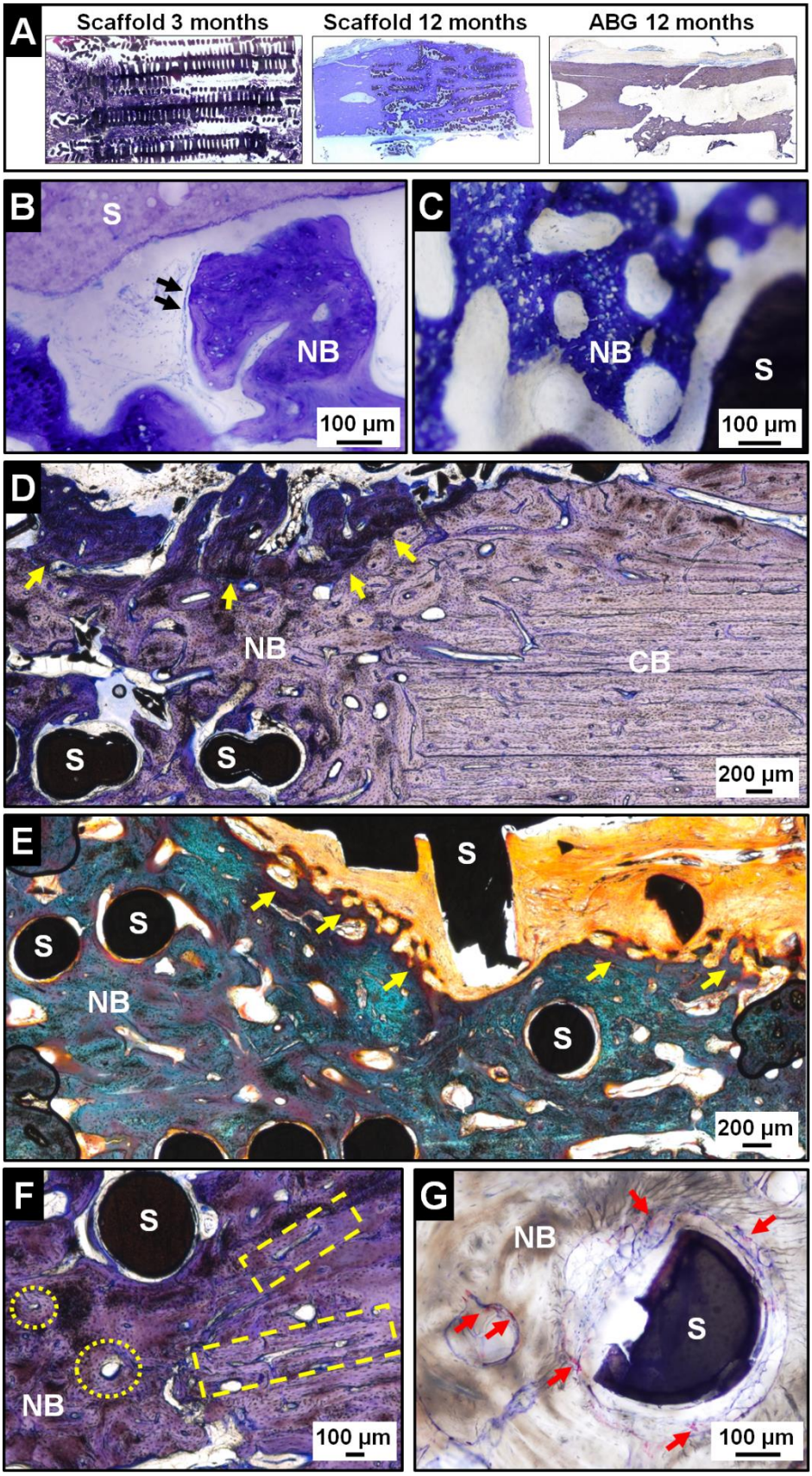

Figure 3. Histological assessment of new bone within the treated defects at 3 and 12 months. Sections were stained with toluidine blue unless otherwise specified. NB = new bone, CB = original cortical bone, S = scaffold. **(A)** Representative whole sections showing defects implanted with the Sr-HT-Gahnite scaffold at 3 and 12 months, and autologous bone graft (ABG) at 12 months. **(B, C)** At 3 months post-implantation, bone tissue within the scaffold was

mostly immature woven bone, with evidence of active bone formation and osteoid (black arrows) lining the new bone. **(D–G)** At 12 months post-implantation, large areas within the scaffold were filled with mature mineralized bone. **(D)** The interface between original cortical bone and newly formed bone showed a transition from highly organized to more randomly orientated lamellar bone (purple). An advancing front of bone formation (yellow arrows) was progressing upwards to fill spaces within the scaffold, containing newly formed mineralized bone (dark purple) lined by osteoid (dark blue borders). **(E)** Goldner's trichrome stain showing mineralized bone (teal) within the scaffold, also with an advancing front of bone formation (yellow arrows) lined by osteoid (dark orange), which was invading upwards into the loose connective tissue (light orange). **(F)** New bone within the scaffold had undergone secondary remodeling to form osteons with a central Haversian canal, the longitudinal (yellow rectangles) and transverse (yellow circles) sections were evident. **(G)** Tartrate-resistant acid phosphatase (TRAP) staining (red) showed osteoclast-specific activity localized in the bone surrounding the scaffold (red arrows), suggesting active remodeling.

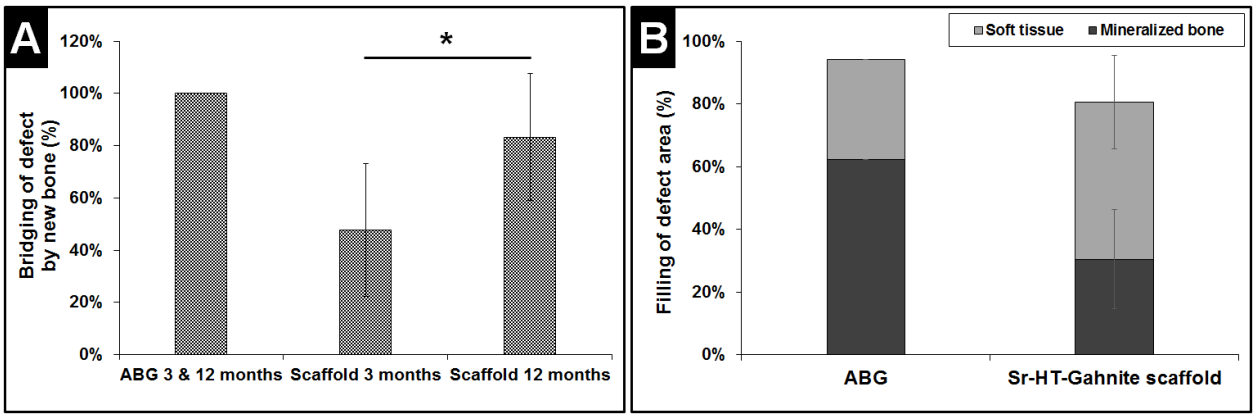

Figure 4. Histomorphometric analysis of bone bridging and composition of new tissue within the treated defects. Goldner's trichrome stained sections were used to analyze samples containing the Sr-HT-Gahnite scaffold (n=8 at 3 months, n=7 at 12 months) or ABG (n=2). **(A)** Percentage of the defect length bridged by new bone for the scaffold and ABG groups at 3 and 12 months. *$p < 0.05$, two-tailed t-test. **(B)** Composition of new tissue within the defect area for the scaffold and ABG groups at 12 months, expressed as percentages occupied by soft tissue and mineralized bone.

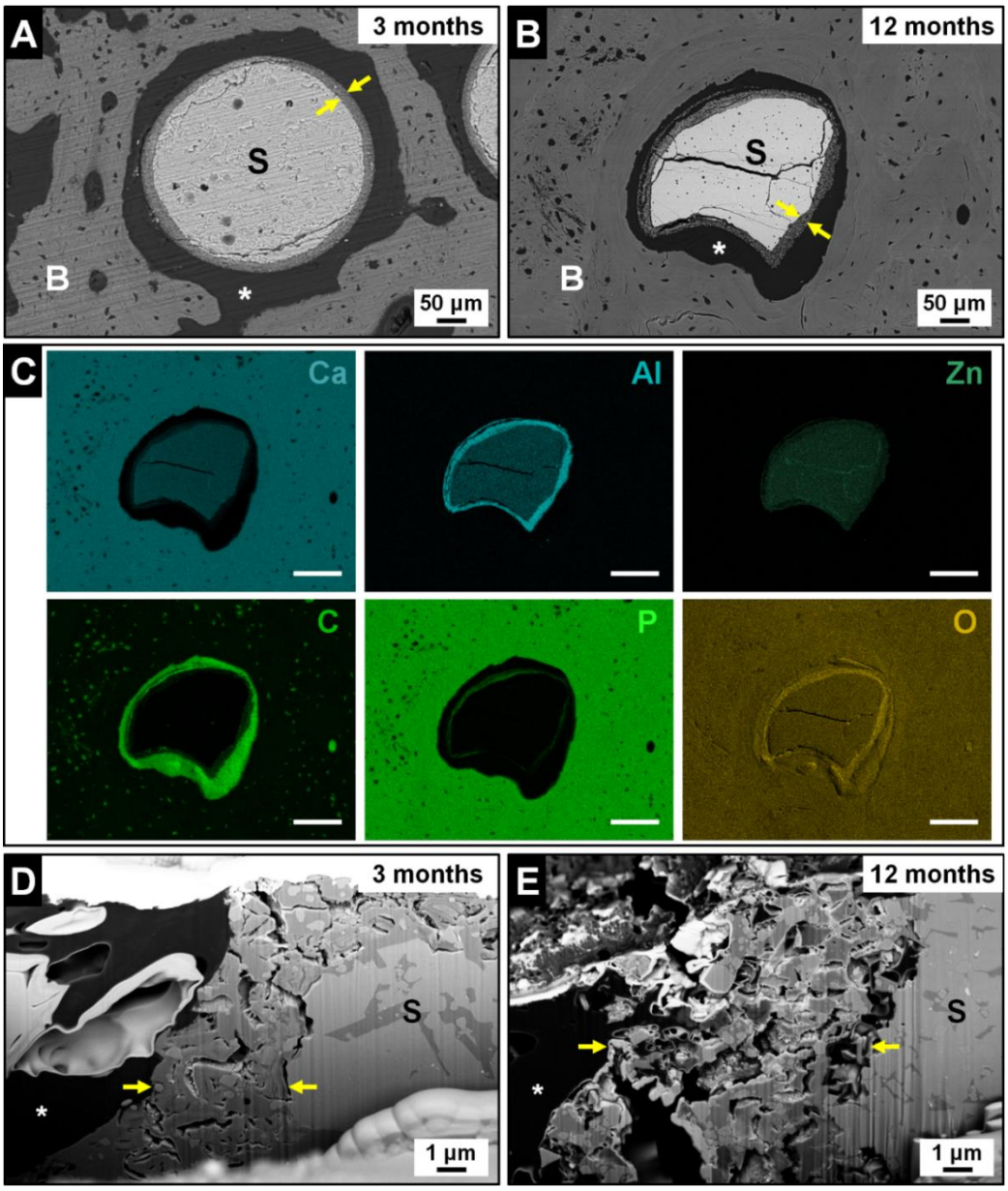

Figure 5. Focused ion beam scanning electron microscopy (FIB-SEM) analysis of sample sections containing the Sr-HT-Gahnite scaffold at 3 and 12 months. B = new bone, S = scaffold strut, * = loose connective tissue. **(A, B)** Lower magnification images showing newly formed bone and loose connective tissue surrounding the scaffold strut, which had a darker border indicative of ceramic degradation (between yellow arrows). **(C)** Elemental maps of the image in (B), showing the distribution of Ca, Al, Zn, C, P and O. Scale bar = 100 µm. **(D, E)** FIB-SEM cross-sections of the implant-bone interface, showing details of the scaffold strut and loose connective tissue, between which was a disrupted border (between yellow arrows) representing a zone of ceramic disintegration. At 12 months, this border became more prominent and was infiltrated by loose connective tissue.

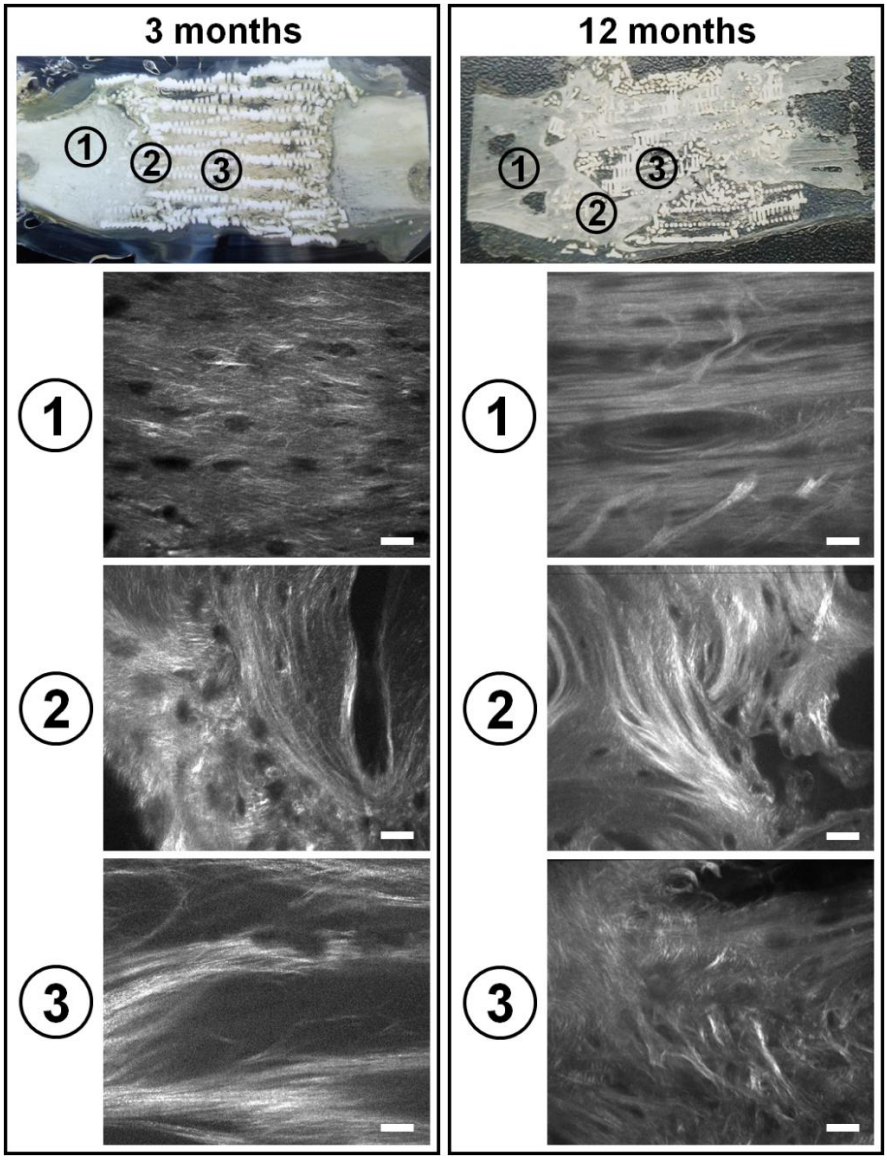

Figure 6. Multiphoton microscopy analysis of sample sections containing the Sr-HT-Gahnite scaffold at 3 and 12 months. Images show the morphology and distribution of collagen type I fibers at different implant locations: (1) in the original bone, (2) within the implant near the defect edge, and (3) within the implant near the middle of the defect. Scale bar = 20 μm.

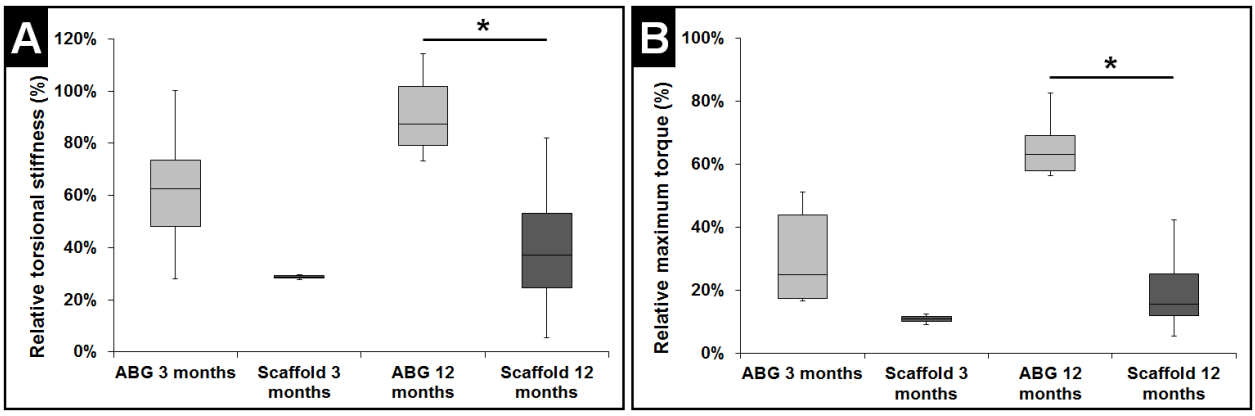

Figure 7. Biomechanical properties at 3 and 12 months. **(A)** Torsional stiffness and **(B)** maximum torque were determined for tibial samples implanted with the Sr-HT-Gahnite scaffold (n=2 at 3 months, n=7 at 12 months) or ABG (n=6), and normalized against values obtained for the contralateral, intact tibia. *$p < 0.05$, two-tailed t-test.

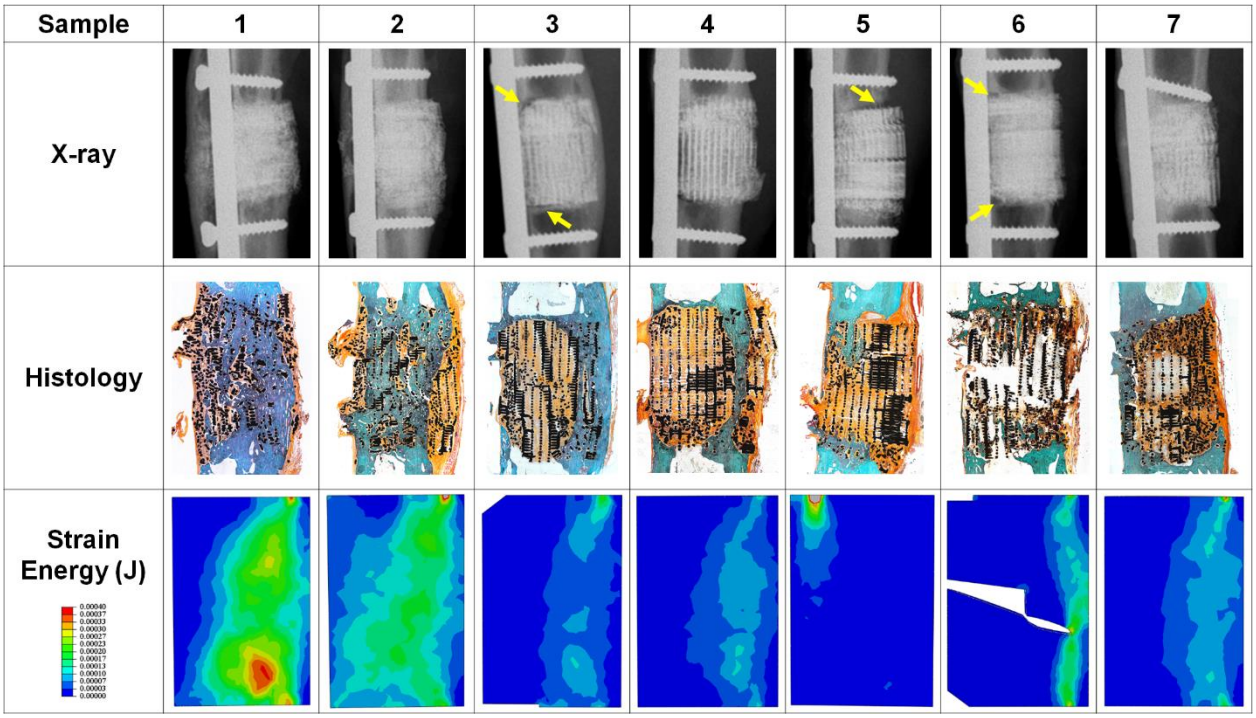

Figure 8. Mathematical modeling of total strain energy for defects implanted with the Sr-HT-Gahnite scaffold at 12 months post-implantation. X-ray images show the arrangement of the fixation plate and screws, and the bone-implant interface (yellow arrows = gaps) in each animal (top panel). Histological images of whole sections stained with Goldner's trichrome (middle panel) are included for comparison with the numerical results of total strain energy in the longitudinal cross-section at the center of each scaffold (bottom panel).

Sr-HT-Gahnite scaffolds showed strong ability to repair large and load-bearing defects in the long bones of sheep over one year, without the addition of cells or growth factors. These 3D printed bioactive ceramic implants may be useful as purely synthetic bone substitutes to augment the clinical treatment of challenging bone defects.

Keywords: ceramic scaffolds, critical-sized bone defects, bone regeneration, bone graft substitutes, gahnite

Jiao Jiao Li, Colin R. Dunstan, Ali Entezari, Qing Li, Roland Steck, Siamak Saifzadeh, Ameneh Sadeghpour, John R. Field, Austin Akey, Martin Vielreicher, Oliver Friedrich, Seyed-Iman Roohani-Esfahani, Hala Zreiqat*

A Novel Bone Substitute with High Bioactivity, Strength and Porosity for Repairing Large and Load-Bearing Bone Defects

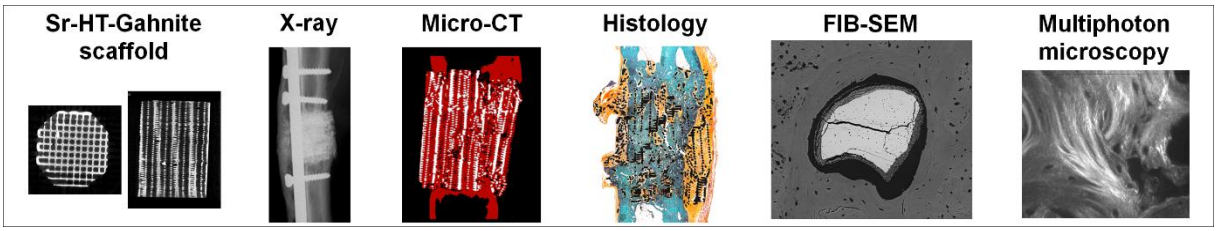

110 mm broad × 20 mm high

Supporting Information

A Novel Bone Substitute with High Bioactivity, Strength and Porosity for Repairing Large and Load-Bearing Bone Defects

*Jiao Jiao Li, Colin R. Dunstan, Ali Entezari, Qing Li, Roland Steck, Siamak Saifzadeh, John R. Field, Austin Akey, Martin Vielreicher, Oliver Friedrich, Seyed-Iman Roohani-Esfahani, Hala Zreiqat**

Supplementary Experimental Section

Mathematical modeling of strain energy: An intact sheep tibia was scanned to reconstruct the μ-CT based tibia model required for the numerical analyses. Reconstructed images were imported into the image-processing software ScanIP (Simpleware Ltd, Exeter, UK). A proper threshold range for bone segmentation was selected by careful inspection of the grayscale images. A Recursive Gaussian filter with 32 μm was applied as a typical smoothing tool. A surface model was created from the segmented bone and saved as a STL file, which was imported into Space Claim (SCDM 17.0) for converting the surface model into a solid model.

Finite element analyses (FEA) were performed using ABAQUS 6.13 (SIMULIA, Providence, RI, USA). The numerical models were created to closely mimic the *in vivo* implantation of the scaffold in each animal. The location of the scaffold and arrangement of the fixation plate and screws were determined from X-ray images taken at 12 months post-implantation. The X-ray images indicated that in most samples, all of the screws were locked and were not able to slide in the grooves of the plate, thereby creating rigid fixation. However, a portion of the screws in some of the samples were free to slide in the grooves of the plate, which were modeled by assuming a friction coefficient of 0.5 between the screw and the plate in FEA. The X-ray images were also carefully inspected to identify any fractures or defects in the scaffolds, which

could have changed the load transfer and affected their contact with the surrounding tibial bone. These structural imperfections were considered when in the corresponding finite element models and analyses.

For each sample, the distal end of the μ-CT reconstructed tibia model was fixed, and a total force of 300 N was applied on the tibial condylar surface to simulate walking condition.[34] A mid-shaft defect (3 cm long) was created to match the *in vivo* defect location. The computer aided design (CAD) model of the scaffold (3 cm high) was designed to reflect the geometry of actual scaffolds used for *in vivo* implantation. The geometry of the plate and screws were modeled from careful measurements of the actual plate and screws used *in vivo*. To balance the accuracy and efficiency of the finite element modeling, a mesh convergence analysis was conducted to determine the size of 4-node linear tetrahedron elements. The cortical bone was assumed to be homogenous and isotropic, with Young's modulus of 19.6 GPa.[35] The plate and screws were made of stainless steel, with Young's modulus of 180 GPa. The base material of the scaffolds (Sr-HT-Gahnite) was assumed to be isotropic, with Young's modulus and Poisson's ratio of 33 GPa and 0.36, respectively.[36]

To reduce computational costs, detailed scaffold models were replaced with homogeneous solid models of the same size, with equivalent (effective) anisotropic material properties.[37] Since the 3D printed scaffold was a periodic structure made by the repetition of a representative volume element (RVE), an asymptotic homogenization technique based on periodic boundary conditions was adopted to determine the equivalent (effective) anisotropic material properties of the scaffolds. The primary idea of the asymptotic homogenization refers to averaging the field variable, such as displacement, within a RVE Ω, which periodically extends itself in space to predict the effective physical properties.[38] For an elastic problem, the deformation is asymptotically expanded to a polynomial as a Taylor series:

$$\mathbf{U}(\mathbf{x},\mathbf{y}) = \varepsilon^0\mathbf{U}^0(\mathbf{x}) + \varepsilon^1\mathbf{U}^1(\mathbf{x},\mathbf{y}) + \varepsilon^2\mathbf{U}^2(\mathbf{x},\mathbf{y}) + \cdots \quad (1)$$

where $\mathbf{U}^0$, $\mathbf{U}^1$ and $\mathbf{U}^2$ represent the field in the 0th, 1st and 2nd order, and are for the small but positive scale factor $0 < \varepsilon << 1$. The microscopic (local) coordinate system and macroscopic (global) coordinate system are given by $\mathbf{x} = [x_1, x_2, x_3]^T$ and $\mathbf{y} = [y_1, y_2, y_3]^T$, respectively. The effective elastic tensor is given by:[39]

$$D^H_{ijkl}(\rho) = \frac{1}{|\Omega|}\int_\Omega D_{ijmn}(\rho)\left[\varepsilon^{0(kl)}_{mn} - \varepsilon^{*(kl)}_{mn}\right]d\Omega \quad (2)$$

where $|\Omega|$ is the volume of the 3D RVE; D_{ijmn} is the elasticity tensor of the base material (Sr-HT-Gahnite); ρ is the volume fraction of solid phase within a local finite element centered at a point $x \in \Omega$ (thus solid and void elements are represented as $\rho = 1$ and $\rho = 0$, respectively, in this framework); and $\varepsilon^{0(kl)}_{mn}$ are linearly independent unit test strains applied to the RVE to determine the characteristic strain fields, $\varepsilon^{*(kl)}_{mn}$. Six test strains were applied, and the characteristic strain can be obtained from the following equation:

$$\int_\Omega D_{ijmn}\varepsilon_{ij}(\nu)\varepsilon^{*(kl)}_{mn}d\mathbf{x} = \int_\Omega D_{ijmn}\varepsilon_{ij}(\nu)\varepsilon^{0(kl)}_{mn}d\mathbf{x} \quad (3)$$

The analysis was conducted on the commercial FEA code ANSYS platform with Parametric Design Language (APDL). Periodic boundary conditions were imposed by designating the opposite nodes with the same nodal number.

Supplementary Figures

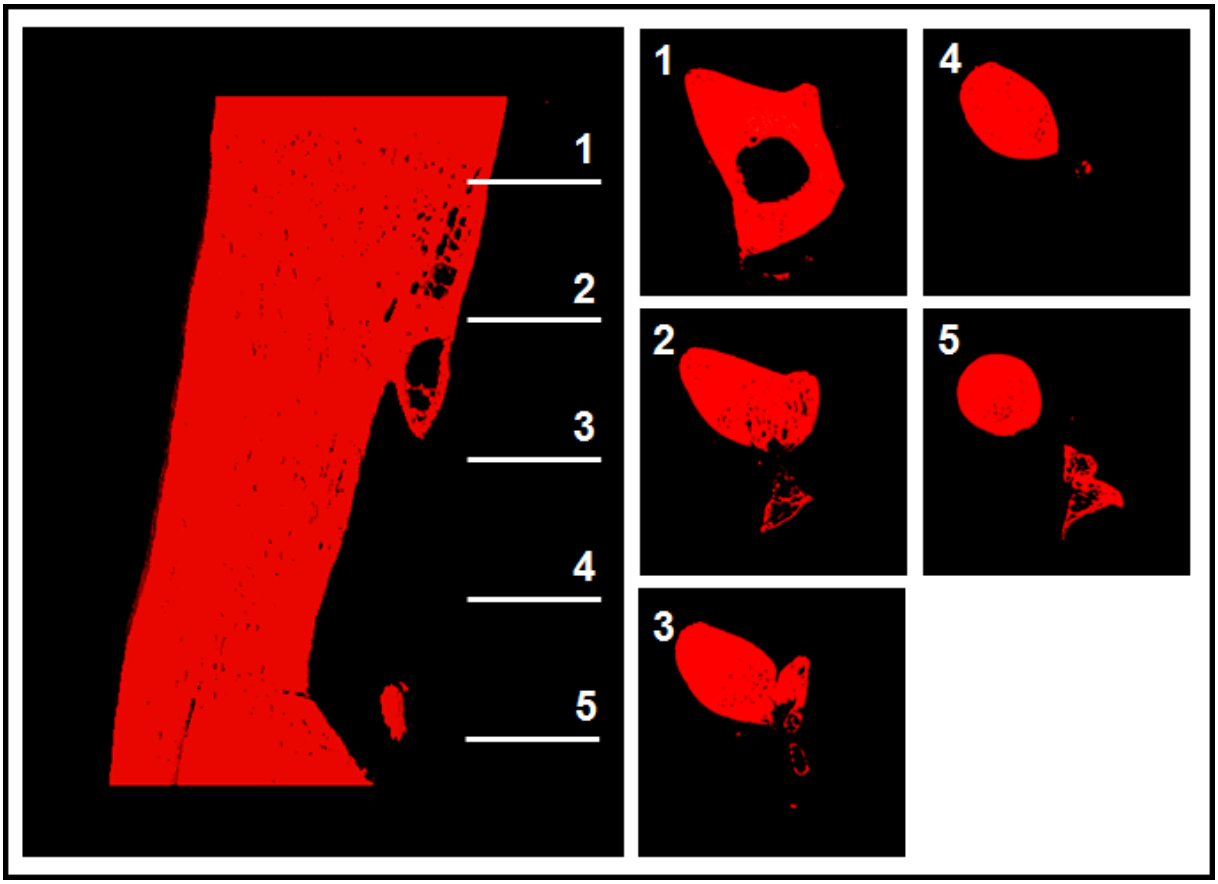

Figure S1. Representative μ-CT image reconstruction of a tibial defect implanted with autologous bone graft at 3 months post-implantation. Complete bridging of the defect, similar to that shown in this figure, was achieved in all samples implanted with autologous bone graft at both 3 and 12 months. Red = bone.

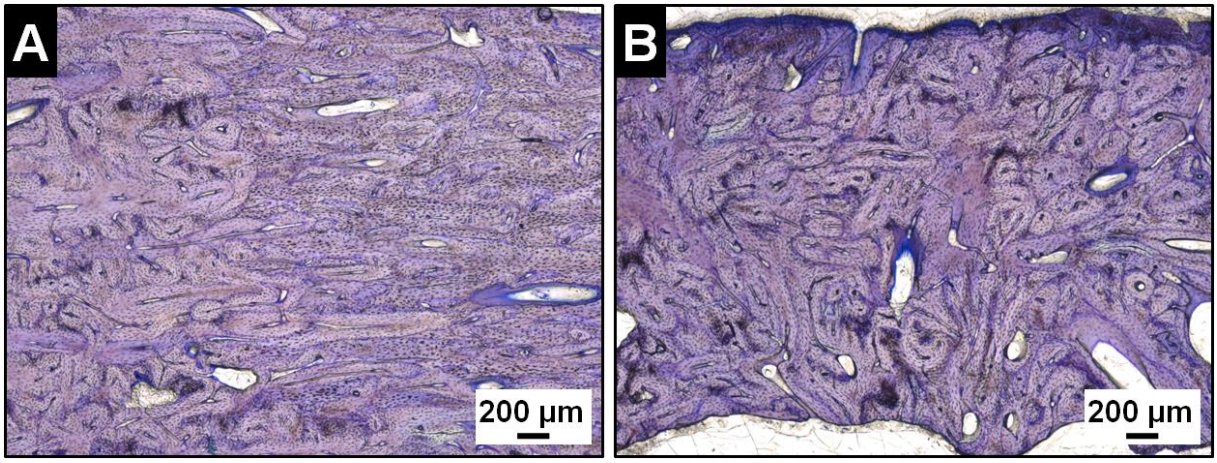

Figure S2. Histological images of defects implanted with autologous bone graft at 12 months post-implantation, stained using toluidine blue. **(A)** The interface between original cortical bone (right) and newly formed bone (left) was not clearly distinguishable. New bone near the defect edge was highly mineralized and not undergoing active remodeling. **(B)** New bone in the middle of the defect was highly mineralized but had a more disorganized appearance. There was some evidence of remodeling and a thin border of ongoing bone formation at the top of the image.

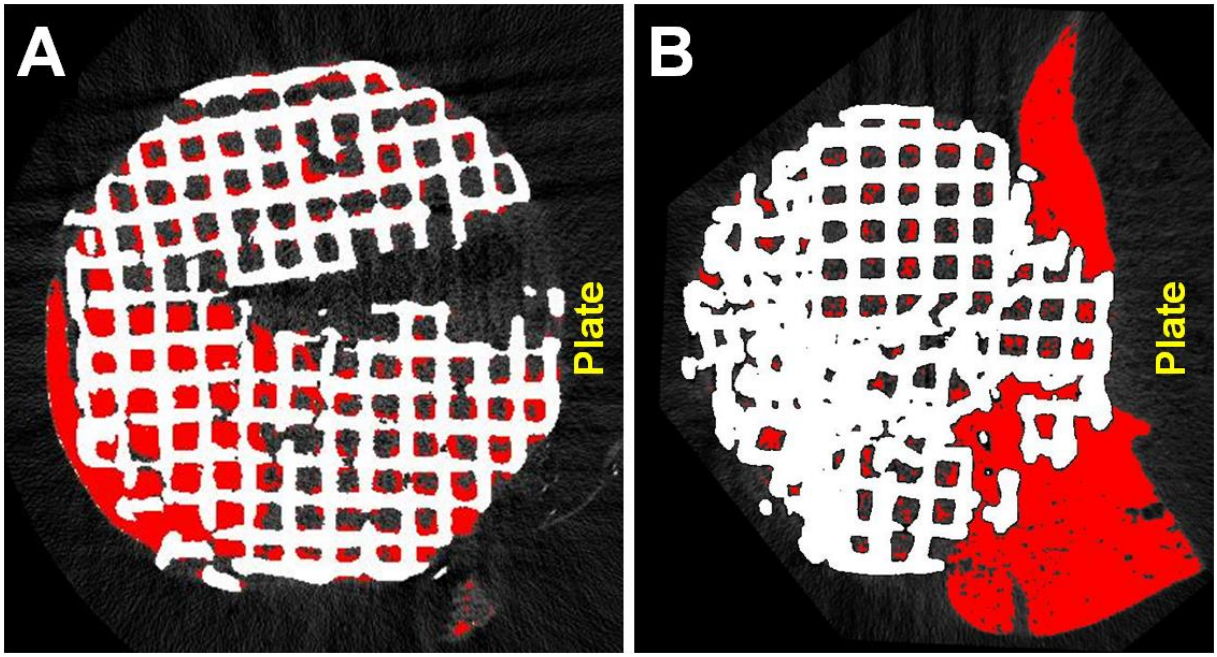

Figure S3. Transverse μ-CT cross-sections for **(A)** sample 6 and **(B)** sample 7 from Figure 8, taken from the middle of the sample. Despite significant bone formation in these samples, the bone was not present in the center plane in the longitudinal direction, leading to minimal bone formation being observed in the histological sections. Red = bone, white = scaffold.

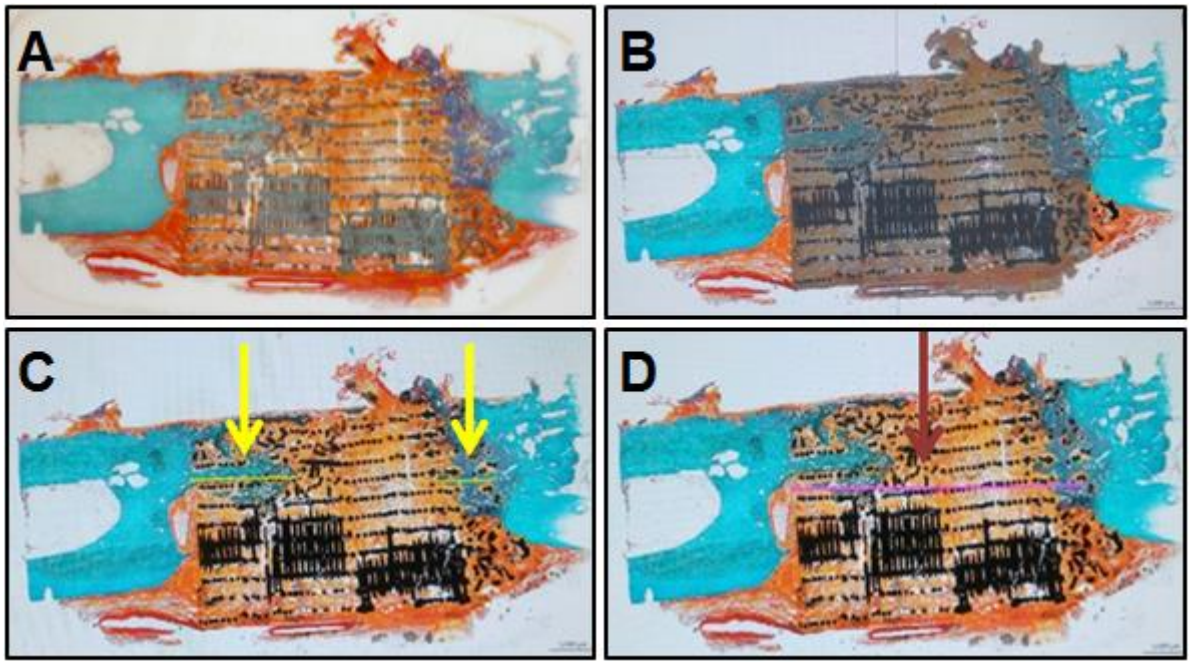

Figure S4. Method of conducting histomorphometric analysis using Osteomeasure. **(A)** Sample sections were stained using Goldner's trichrome (orange = soft tissue, teal = mineralized bone). **(B)** The defect area (grey) was selected by defining the proximal and distal defect boundaries. **(C)** If bone bridging was incomplete, the distance of penetration into the defect area (yellow lines) by newly formed mineralized bone was measured from both the proximal and distal defect boundaries. **(D)** The total length of the defect area (pink line) was then measured to calculate the percentage of bone bridging across the defect.

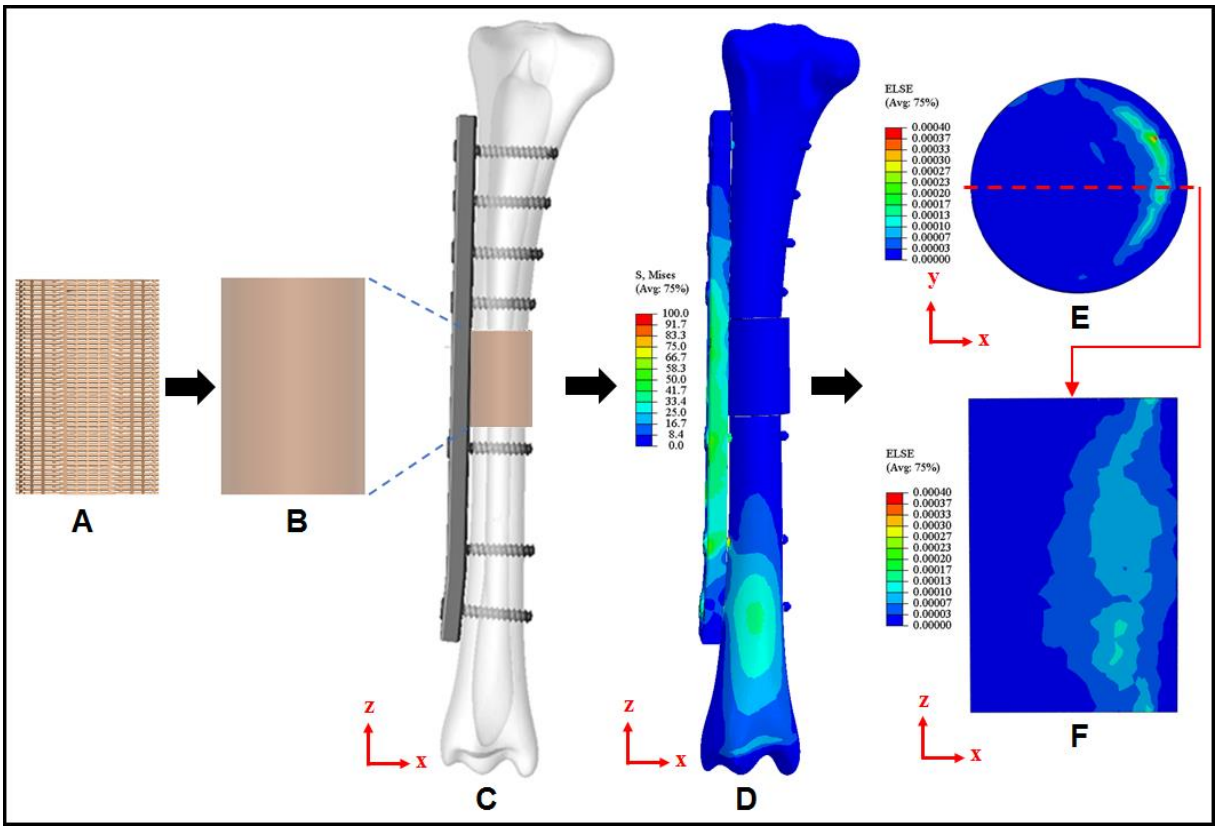

Figure S5. Mathematical modeling to determine total strain energy in the Sr-HT-Gahnite scaffolds. **(A)** The computer aided design (CAD) model of a porous scaffold. **(B)** A solid block having homogenized material properties equivalent to the porous scaffold. **(C)** The CAD model of a scaffold implanted into a 3cm defect in sheep tibia, stabilized using fixation plate and screws. **(D)** The contour of von Mises stress distribution in the model. **(E)** The contour of total elastic strain energy in the scaffold. **(F)** The contour of total elastic strain energy in a cross-section located at the center of the scaffold.